Geographically constraining the South Australian Heat Flow Anomaly

Thesis submitted in accordance with the requirements of the University of Adelaide for an Honours Degree in Geophysics.

Henry Oscar Johnson

November 2014

THE UNIVERSITY
of ADELAIDE

ABSTRACT

The South Australian Heat Flow Anomaly is a large contiguous region of anomalously high heat flow ($>$90 mWm^{-2}) in otherwise tectonically quiescent Proterozoic lithosphere. The broad anomaly ($>$400 km) is nearly 40 mWm^{-2} greater than the global average for terranes of similar tectonic age, but is poorly constrained geographically due to relatively few and poorly distributed heat flow data. This study reports four new heat flow determinations, located to improve the spatial sampling. The product method and thermal resistance were used to calculate heat flow.

Data were obtained from drillhole core samples that traverse the anomaly. The samples were then scanned for thermal conductivity using a Thermal Conductivity Scanner. Temperature logs of the drillhole are used to determine the thermal gradient with depth. The product of thermal conductivity and thermal gradient determines surface heat flow.

The spatial extent will become better defined with each new heat flow datum as well as increase the confidence of the pre-existing data source of the anomalously high heat flow was ascertained by evaluating bias in previous data measurements, recent tectonic and magmatic activity. Using existing data and measurements made in this study, evidence for and against a primarily deep mantle and shallow crustal radiogenic source will be examined.

KEYWORDS

Heat Flow, Thermal Conductivity, South Australia, Anomaly, Drillholes

Table of Contents

List of Figures

List of Tables

INTRODUCTION

The South Australian Heat Flow Anomaly (SAHFA) is an area of anomalously high heat flow, 92 $\pm$10 mWm^{-2} (Neumann et al., 2000), trending N-S along the Adelaide Fold Belt (AFB). The SAHFA is bordered by the Gawler Craton to the west and the Murray Basin and Curnamona Province to the east (Figure 1). The SAHFA is considered to have anomalously high heat flow compared to the average for global Proterozoic provinces, 49 mWm^{-2} to 54 mWm^{-2} (Chapman & Furlong, 1977; Morgan, 1984; McLaren et al., 2003; Thakur & Blackwell, 2006).

In this paper a craton is defined as a region of the Earth's crust that has remained relatively stable for several hundred million years Preiss et al. (2002). All cratons consist of belts that were mobile prior to cratonisation, which is the result of devolatilisation and petrologic depletion (Pollack, 1986). Similar to a craton, a province is a general term which is given for a regional scale body of rocks within the Earth's crust. It has a specified spatial and temporal extent and some other broader unifying geological characteristics but has not seen recent tectonism.

The exact extent of the SAHFA is poorly defined due to few and sparse sampled heat flow data (Matthews & Beardsome, 2007). Improving heat flow coverage will allow mapping of different lithospheric domains, identifying areas of anomalous uranium that map out alteration systems such iron-oxide, copper, gold, uranium and rare earth element (IOCG) systems, analogous to that of Olympic Dam (Hand et al., 2007). In addition to improving geographic coverage, improved estimates of heat flow will provide better constraints on the distribution of heat producing elements within the upper crust.
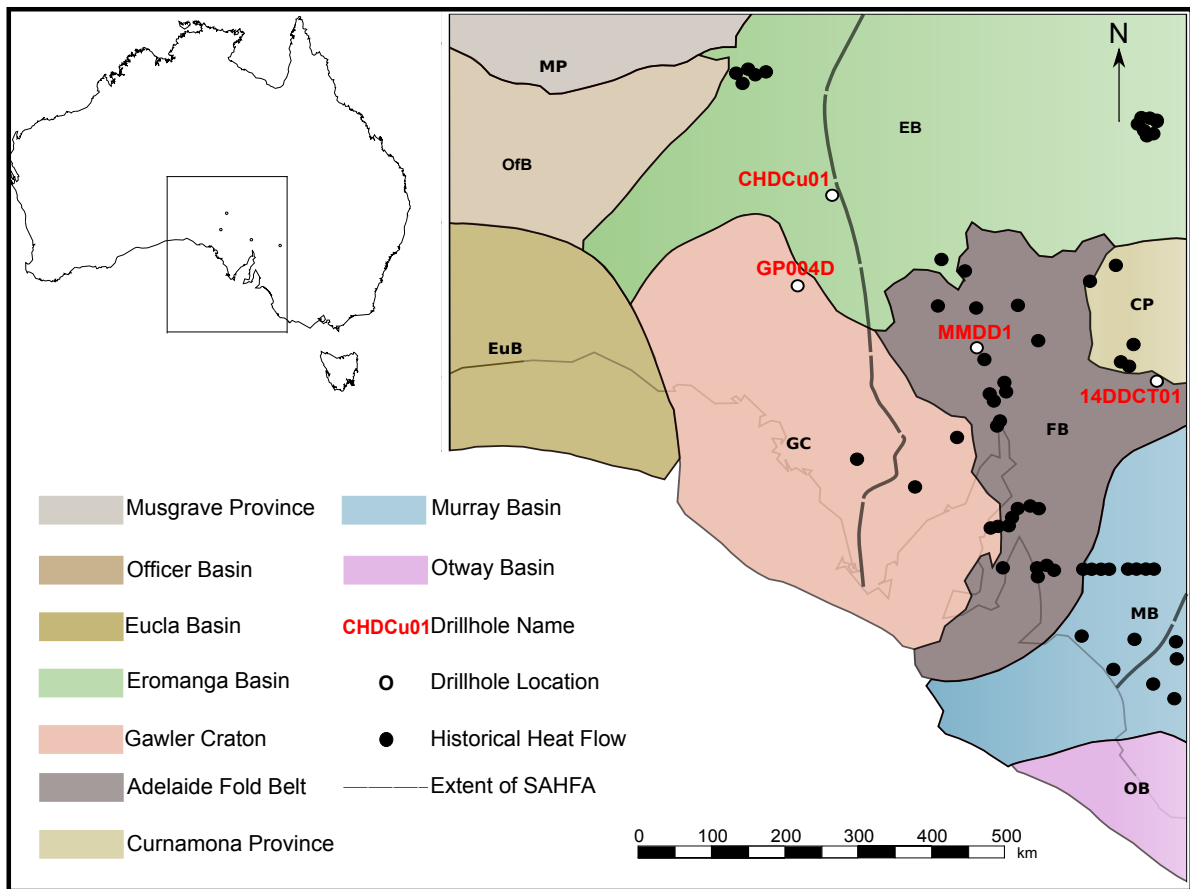
Figure 1: Key geological provinces in South Australia and locations of heat flow sites compiled by D. Hasterok (pers. comms. 2014). Heat flow measurements made in this study are depicted as open circles. Dashed lines indicate current extent of the SAHFA.

Authors from previous studies have suggested the most likely cause of the SAHFA is high upper crustal heat production associated with granites enriched in U, Th and K (Houseman et al., 1989; Hand & Wyborn, 1999; McLaren et al., 2003). If high heat production is the cause a high surface heat flow magnitude would be expected ($\sim$90 mWm^{-2}) (Neumann et al., 2000), as well as a short, lateral heat flow gradient. The shape of the anomaly shown would be restricted to tectonic terranes, basins and plutons. In areas of thick crust we expect a high heat flow due to an increase of heat producing radiogenic elements. If the SAHFA is in an area with a thin lithosphere, the

boundary between the asthenosphere and lithosphere will be closer to the surface and hence a high surface heat flow would be expected.

In this paper, four new heat flow determinations in localities that traverse South Australia are reported, in an effort to improve the regional heat flow field and better characterise the spatial extent of the SAHFA. The new sites are in locations with few pre-existing data or fill spatial gaps in the South Australian dataset, which assists in the identification of high heat producing areas and helps constrain the SAHFA geographically. New heat flow determinations, from the rocks thermal properties are made from temperature profiles in four drillhole, and thermal conductivity measurements taken within these drillhole. The new sites are in locations with few pre-existing data or fill spatial gaps in the South Australian dataset, which assists in the identification of high heat producing areas and helps constrain the SAHFA geographically.

BACKGROUND

HEAT FLOW

Heat flow within the mantle has been measured over much of the Earth's surface, cumulating in over 20,000 data points which gave a global mean of 65 mWm^{-2} (Pollack et al., 1993), which is greater than 56 mWm^{-2} which Michaut & Jaupart (2009) obtained. Pollack et al. (1993) also categorised the statistical heat flow averages based upon age and prevailing regional geology.

Surface heat flow Q_s is represented by,

$$Q_s = k \cdot \frac{\Delta T}{\Delta Z},$$
(1)

where,k is the thermal conductivity of a drillhole, which is the ability to conduct heat, and $\frac{\Delta T}{\Delta Z}$ is the thermal gradient from bottom to top of hole. Variations in Q can be attributed to variations in heat coming from below the lithosphere, q_b, and heat actively generated by crustal radiogenic elements, q_c (McLaren et al., 2003).

GEOLOGICAL SETTING

The AFB is a Neoproterozoic to Middle Cambrian basin with a history of five rift cycles (Preiss, 2000). The most recent activity and the causation of the distribution of present day rock units was the Delamerian orogeny (Clifford et al., 2008). Another significant event was a period of extension beginning in the Paleozoic which led to the formation of the Gawler and Curnamona province(Stewart & Betts, 2010).

The Gawler Craton (late Archaean-early Mesoproterozoic) and Curnamona Province (Palaeo-Mesoproterozoic) are two large complex basement terranes consisting of mafic and felsic igneous intrusions and volcanics and minor unmetamorphosed sedimentary deposits (Preiss et al., 2002). Mesoproterozoic granites, felsic volcanics and gneisses in the Gawler Craton and Curnamona Province contain anomalously elevated uranium and thorium concentrations relative to global Proterozoic averages (Neumann et al., 2000) and generate high heat flows. The central and northern part of the SAHFA have been covered by Neoproterozoic, Palaeozoic, Mesozoic and Tertiary sediments.

In the South Australia's northeast, Mid-Carboniferous granite (Big Lake Suite) has been covered by the Cooper, Eromanga and Lake Eyre basins. While this granite has lower heat production when compared to the Gawler Craton and Curnamona Province granites, it is blanketed by over 3 km of insulating Late Carboniferous-Recent sandstone, siltstone, shale and coal (Robertson et al., 1998). This has effectively trapped

4

heat generated from the granite at temperatures of 250°C at 4.5 km depth.

DRILL HOLE DESCRIPTIONS

14DDCT001

Drillhole 14DDCT001 intersected a sequence of psammites and calc-silicates with disseminated and thin veinlets of pyrrhotite (pyr) and pyrite(py). Minor Cu and Zn in the form of chalcopyrite (cp) and sphalerite is associated with the veining, hosted within pegmatite.

CHDCu001

A drillhole used for mineral exploration with a bottom of hole (BOH) of 550.1 m. From where the sampling started at 102.1 m until 287.5 m; quartz (qtz), potassium feldspar (k-feld), biotite (bt) and chlorite (cl) which defines the foliation, were all present.The interval, 287.5 - 360.9 m, consists of a qtz and k-feld gneiss with associated metallic oxides (garnet, magnetite) often occurring in laminations. From 360.9 m to BOH the gneissic fabric becomes intermittent with massive potassium feldspar and quartz throughout.

GP004D

Hole drilled for mineral exploration to a depth of 697.5 m, temperature logging was only present from 0 to 425.5 m. The Beda Volcanics are once again present, however below the depth of which was temperature logged. Calcareous mudstone, sandy lenses and qtz veins are evident throughout which form the Woocalla Dolomite (Lambert et al., 1971) as well as the Whyalla Sandstone. No data were available for 0 - 425.5 m. Intermediary intervals were determined from points of inflection of the temperature and depth data.

MMDD1

The interval of sampling was from 307.2 to 690.2 m. From 307.2m until 369 m the Whyalla sandstone was present (Williams, 1998). There was then a transition into the Woocalla Dolomite (Lambert et al., 1971) and then another transition into the Tindelpina formation at 417 m. This was a particularly large unit, extending for 160 m. From here to the end of sampling it consisted of the Beda Volcanics (Webb & Horr, 1978)

METHODS

Drillholes

Drillholes which were specifically drilled for mineral exploration were used to calculate heat flow. The drillhole had to be in the regional locale of the SAHFA and must have associated temperature data and accessible core suitable for thermal conductivity analysis. The drillhole were surveyed by Endeavour Geophysics using a Multi-Survey tool instrument. Temperature was recorded every 0.01 m.

Thermal gradient

The thermal gradients between successive points were calculated by finding the difference in temperature, over the difference in distance. Temperature and thermal gradient were plotted versus depth and areas of constant gradient were noted. Constant gradient was indicative of where core samples should be scanned for thermal conductivity, further enhancing the sampling plan. Constant gradient was desirable as this represents a zone of constant thermal conductivity,assuming a conductive regime with minimal heat generation.

Reduced temperature, T_R, was computed also. T_R is an artefact of the paleoclimate and shows the effect of temperature changes that take place slowly over Earth's history. It is calculated by finding the slope of temperature versus depth and subtracting this value from the thermal gradient. T_R depths greater than zero indicate regions that are of above what is expected from the thermal gradient.

The thermal gradient was calculated by implementing a moving mean. This effectively windows 'x' data points, computes the mean, then moves the window on again and repeats. The size 'x' of the window is determined independently for each drillhole and is deemed effective when the noise, due to the precision limitations, was removed. The precision limitations occur from the high sampling rate, 0.01 m, of the Multi Survey tool.

Core used for conductivity measurements are stored at the Adelaide Core Library at Glenside or at their overflow warehouse in Thebarton. A walk through of the core was initially done to observe that if the core was in a state that would be suitable to scan using the TCS. Samples are suitable if they are intact and have no obvious large fractures. The sampling strategy which was implemented, was that selections of core were relatively random every 10 m. This was greater in regions of shorter lithological changes. The chosen core was then taken to the University of Adelaide to where the TCS is housed.

Density and porosity

Since *in situ* rocks are typically fluid saturated, thermal conductivity was measured on both unsaturated and saturated core, so that the effects of each can be seen. A relationship on thermal conductivity and interconnected porosity was also examined.

To saturate the core, it was submerged in water into a vacuum oven. The pressure of the vacuum was pumped down to -95 kPa and the core is left to equilibrate and saturate for a minimum of 4 hours. Once the core was removed, it was stored submerged in a bucket of water to ensure the core remained saturated. Core was removed from the bucket only to conduct measurements.

The core was then weighed on an Adam Equipment TBB 2610T triple beam balance with a stated error of 0.1 gram. The core was weighed saturated and unsaturated. It was then suspended via a hook from the balance in a body of water using nylon string. The density and interconnected porosity of the core was calculated using the calibrated displacement method with the equations;

$$V_b = M_{sat} - M_{sub}, \tag{2}$$

$$V_p = M_{sat} - M_{dry}, \tag{3}$$

$$\phi = \frac{V_p}{V_b}, \tag{4}$$

where M_{dry} is the unsaturated weight of the core, M_{sub} is the weight of the core submerged in a body of water, V_p being the pore volume of the rock, V_b bulk volume of the sample and finally ϕ_I, is the interconnected porosity.

Thermal conductivity scanner

A series of theoretical and experimental investigations was carried out by Popov et al. (1999) to evaluate the potential of an optical scanning technique for obtaining values for the thermal properties of core. The optical scanning method is based on scanning a sample surface with two temperature sensors in combination with a focused, mobile and continuously operated constant heat source. The heat source and sensors move with

the same speed relative to the sample at a constant distance to each other. For a more detailed resource see Appendix A.

PREPARATION OF CORE

To prepare the core for scanning on the TCS it had to be painted. A 30-40 millimetre wide, continuous, straight black line using an acrylic, water based, non-transparent, jet-black varnish with a silky matte finish paint was marked down the length of the core. This ensured that variations in reflectivity of the minerals within the sample did not effect the amount of heat input by the optical head. The paint was applied evenly with few to no brushstrokes left behind, at a thickness of $\sim 40\mu$m thick (Bowker, 2013). Samples were allowed to dry for a day before commencing scanning.

SCANNING OF CORE

Standards are used with the TCS so that the sample is normalised against something with a known thermal conductivity value. As seen in Table 1 the standard used is dictated by the thermal conductivity of the sample and the one used should have a similar value. All scanning was undertaken on the long axis of the core. If the core had not been halved, it was propped up by metal spacers to be coincident with the scanning stage.

Table 1: Table of Standards including the material and the respective thermal conductivity

Standard	Material	k $(Wm^{-1}K^{-1})$
1	Glass	0.709
2	Fused Quartz	1.350
3	Gabbro	2.370

4	Titanium Alloy	5.940
5	Steel	13.3
6	Fused Silica	1.389

PROCESSING OF DATA

After the scanning of the core was completed, the values were copied across to an open spreadsheet. Dependant on the diameter of the core (HQ, NQ) and also the value given for k, a correction factor had to be supplemented to the thermal conductivity reading. This correction is needed due to differences in the heat diffusion and cooling dynamics of the halved and diameter core (Bowker, 2013). See Table 2 and 3 for correction factors.

Table 2: Corrections for HQ core given the thermal conductivity of a given sample. Also given is the averaged curved surface error

Sample k range $(Wm^{-1}K^{-1})$	Average curved surface error (%)	Correction Factor
< 4	-5.703	1.057
> 4	-7.056	1.071

Table 3: Corrections for NQ core given the thermal conductivity of a given sample. Also given is the averaged curved surface error

Sample k range $(Wm^{-1}K^{-1})$	Average curved surface error (%)	Correction Factor
< 3.5	-5.144	1.051
> 3.5	-5.614	1.056

Corrections

The thermal gradient and the thermal conductivity profile, which are both cardinal for determining heat flow estimates, come from processes in which we do not have the greatest confidence. After a drillhole has been drilled by either reverse circulation (RC) or diamond drilling (DD), a geophysical log of the drillhole is taken soon after. Even taking into account the error of the temperature probe, temperatures in and around the wells are perturbed by the drilling process, which alters the temperature from in-situ

conditions. **?** devised a method to account for this error, which has allowed for lateral changes in several parameters including surface temperature, thermal conductivity and heat flow. This was unlike Carvalho & Vacquier (1977) who restricted their method to just a singular temperature gradient and solitary thermal conductivity function. The equation for the correction is as follows,

$$k = k_{20} \left(\frac{293}{T + 273} \right). \tag{5}$$

It has to be noted that this equation is for assumed solid matrix (does not take into account porosity). However this correction was still used due to the lowly (¡ 1.4%) interconnected porosity readings which were obtained across the four drillhole (see Appendix D, table 9 through to 12).

Heat flow calculations

The heat flow of a drillhole was determined from the average thermal conductivity $k_a v$ and thermal gradient, $\Delta T \Delta Z$. Obtaining k_{av} was realised through k measurements given from the TCS. These values were used to calculate the harmonic mean of an interval (lithological package), k_i. When k_i was determined for $i = n$, where n equals the number of intervals, the harmonic mean was computed to determine $k_a v$. The thermal gradient was calculated from the bottom hole temperature and to the depth of where climatic effects were negligible, $\frac{\Delta T}{\Delta Z}$. This depth was found from the T_R graphs. Equation 1 was then utilised to calculate the surface heat flow of the drillhole.

Another method which may be used is from the determination of interval heat flow, q_i which is,

$$q_i = k_i \cdot \left(\frac{\Delta T}{\Delta Z} \right) |_i, \tag{6}$$

where $\left(\frac{\Delta T}{\Delta Z}\right)\big|_i$ is the thermal gradient of an interval. q_i was determined for $i = n$, where n equals the number of intervals. The arithmetic mean of all q_i was computed to determine Q.

Errors were associated with the temperature log are assumed to be negligible and thermal conductivity scanner were propagated throughout. This was completed via calculating the derivative of the harmonic mean for thermal conductivity. The value for the error of thermal conductivity were given as an output from the TCS and varied from sample to sample.

The thermal resistance, R, a heat property of a materials resistance against heat flow, of each lithological unit was also measured,

$$R(z) = \int_0^z \frac{\Delta z}{kz'}, \tag{7}$$

which is defined as the integral of the depth range z, over the thermal conductivity k. A plot of R against temperature °C was constructed, which is commonly known as a Bullard Plot (Bullard, 1939). From the constant gradient a heat flow value was determined. Linear regression was used as not all slopes were constant.

Error propagation

Each heat flow value has an associated random error, σ_q. To propagate this error throughout a derivation of the heat flow was imperative. The general form of error propagation is as follows,

$$\sigma_q = \left(\sigma_k^2 \Gamma^2 + \sigma_\Gamma^2 k^2\right)^{\frac{1}{2}}, \tag{8}$$

where, Γ, is the thermal gradient of the entire hole, k, is the harmonic mean of thermal conductivity for the entire hole, σ_k^2, is the error in thermal conductivity and σ_Γ^2, is the error the thermal gradient of the hole.

OBSERVATIONS AND RESULTS

Thermal gradient and reduced temperature

From the thermal gradient it was possible to calculate the reduced temperature (T_R) of the drillhole. The T_R gives a proxy as to a depth to which the paleoclimate has affected the Earth. As a measure of caution all calculations were made using depths greater than 100 m as to make certain the climatic effects did not have bearing in the results.

For drillhole 14DDCT001, the temperature is constant with depth through the entire hole (Figure 2a). Figure 2b corresponds with this as from $\sim$50 to $\sim$425 m the thermal gradient is constant as well which indicates a gradual change in lithologies or even only a few lithologies being present, if edge effects are discounted. The edge effect are due to the windowing process and are minimized with the current window set at 6000, which translates to depths of 60 m. From 2c the T_R passes zero at $\sim$42 m, which indicates that the paleoclimate has affected this area up until a depth of 42 m. This once again corresponds with the infliction and thermal gradient (b). It is noted the first data point for the moving mean was excluded from (b) due to it being an outlier (a value of 166.5).

Drillhole CHDCu01, appears to have two different slopes(Figure 3a). The first is seen from beginning of hole to $\sim$130 m and the second from there to the bottom of hole. This is seen in (b), somewhat clearer, from the means tailing away from the midpoint at $\sim$130 m. Once again edge effects are present due to windowing, to which the effects

Figure 2: An analysis of thermal variations with depth, within drillhole 14DDCT001. Subplots include (a) temperature, (b) thermal gradient and (c) reduced temperature. The original data has also been supplemented with a moving mean and a weighted mean.

were minimised with a window size of 5000. If a smaller window was used (a) and (c) would appear smoother and more linear, while (b) would become noisier. With a window bigger than ∼5500, (b) has all the noise taken out while (a) and (c) had exasperated edge effects. The thermal gradient is similar to Figure 2 as it is constant from ∼30 m to where it tails of slightly to BOH where edge effects have taken over and hence the gradient is moving toward 0 mKm^{-1}. These edge effects are due to the windowing these data which comes from computing the weighted mean. The near surface climatic effect extends ∼90 m (Figure 3c).

Figure 3: An analysis of thermal variations with depth, within drillhole CHDCu001. Subplots include (a) temperature, (b) thermal gradient and (c) reduced temperature. The original data has also been supplemented with a moving mean and a weighted mean.

The drillhole GP004D had a marked difference in thermal properties (Figure 4) compared with drillholes CHDCu001 and 14DDCT001 (Figure 3,2). This is from the consistent change of slope from (a) and (b) which coincides with a change in lithology. 4(a) shows three distinct slopes from top of hole to ∼200 metre, 200 to ∼270 m, and then to BOH. The window size used was 3500 (equates to 35 metre depths), which was the smallest of the previous three figures, but was due to the amount of data that was available for GP004D. The paleoclimate affected this area to a greater depth than the previous three as well (∼130 m).
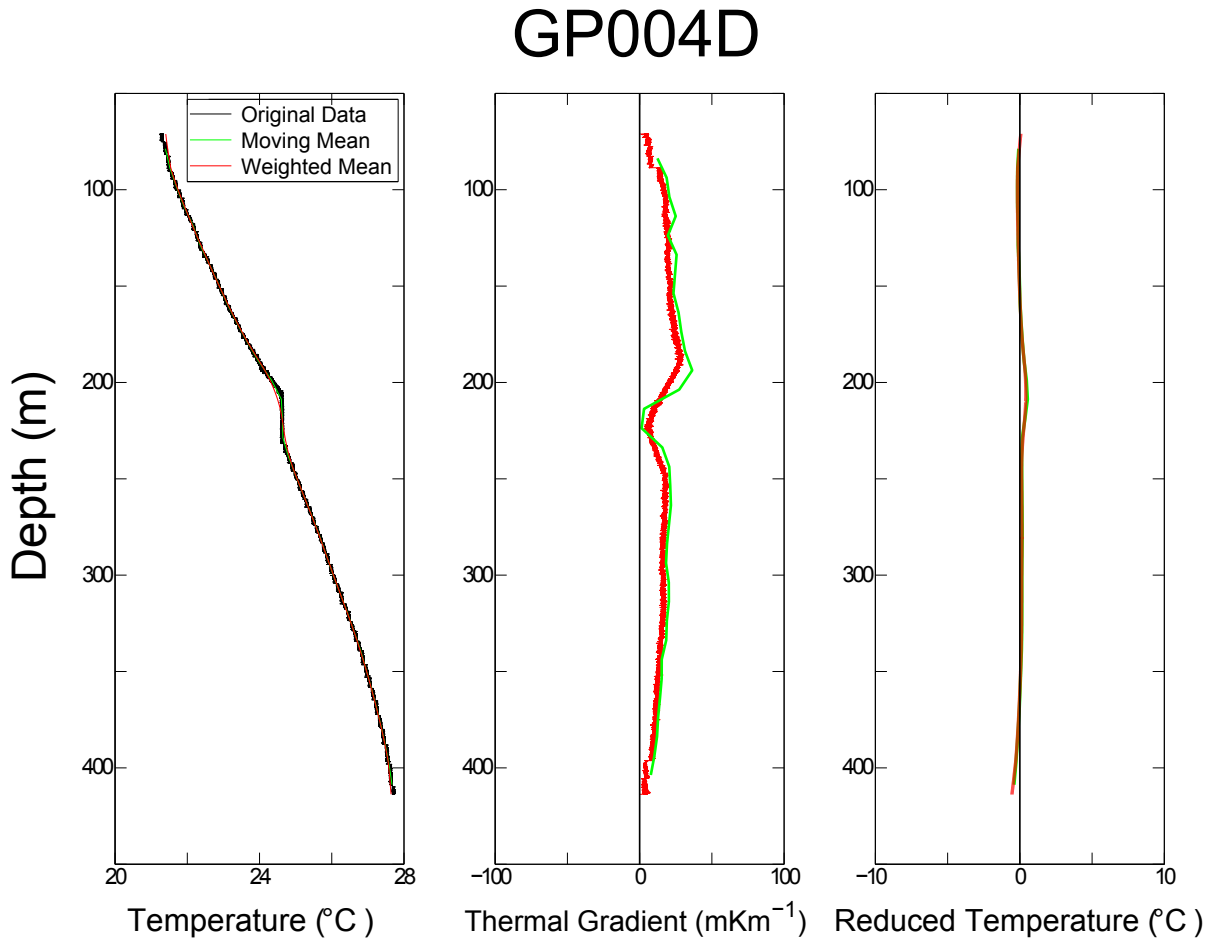
GP004D

Figure 4: An analysis of thermal variations with depth, within drillhole GP004D. Subplots include (a) temperature, (b) thermal gradient and (c) reduced temperature. The original data has also been supplemented with a moving mean and a weighted mean.

Drillhole MMDD1 illustrates the greatest amount of variation out of the four observed drillhole. Figure 5 shows a varying slope in all three subplots. The mineralogical changes in each of the lithologies would account for these erratic changes.

Thermal conductivity

Drillhole 14DDCT001 was interpreted to have five changes in lithology (Figure 6). These lithologies ranged in thermal conductivity from $2.566 \pm 0.077 \mathrm{Wm^{-1}K^{-1}}$ for the psammite with associated iron oxide bands, to $3.143 \pm 0.030 \mathrm{Wm^{-1}K^{-1}}$ for the calc-silicate
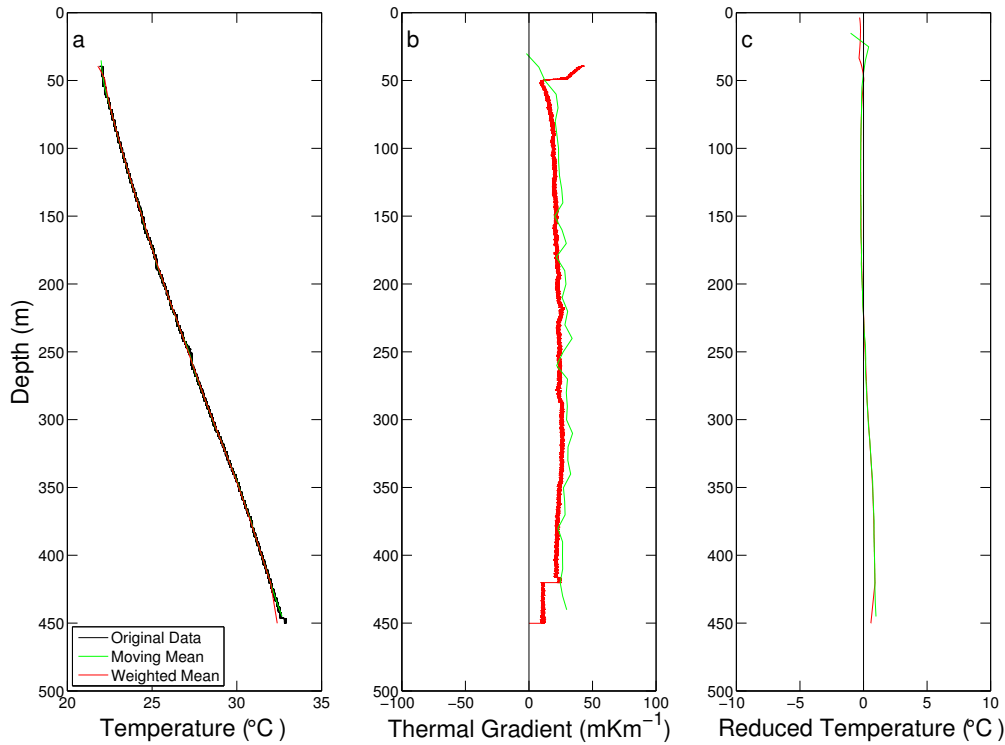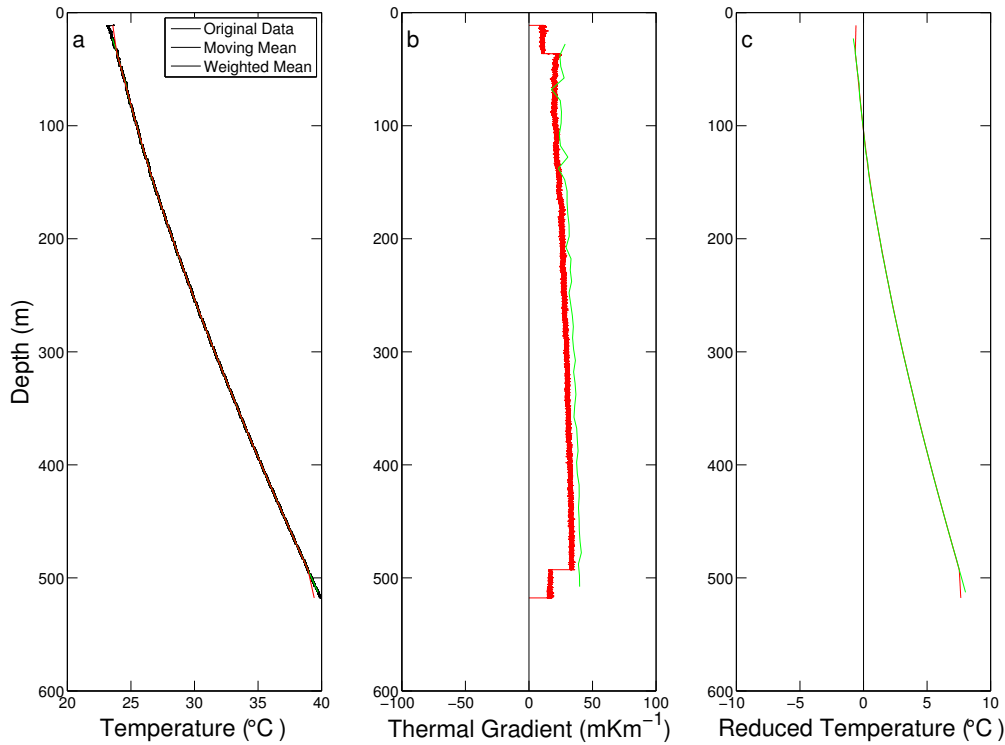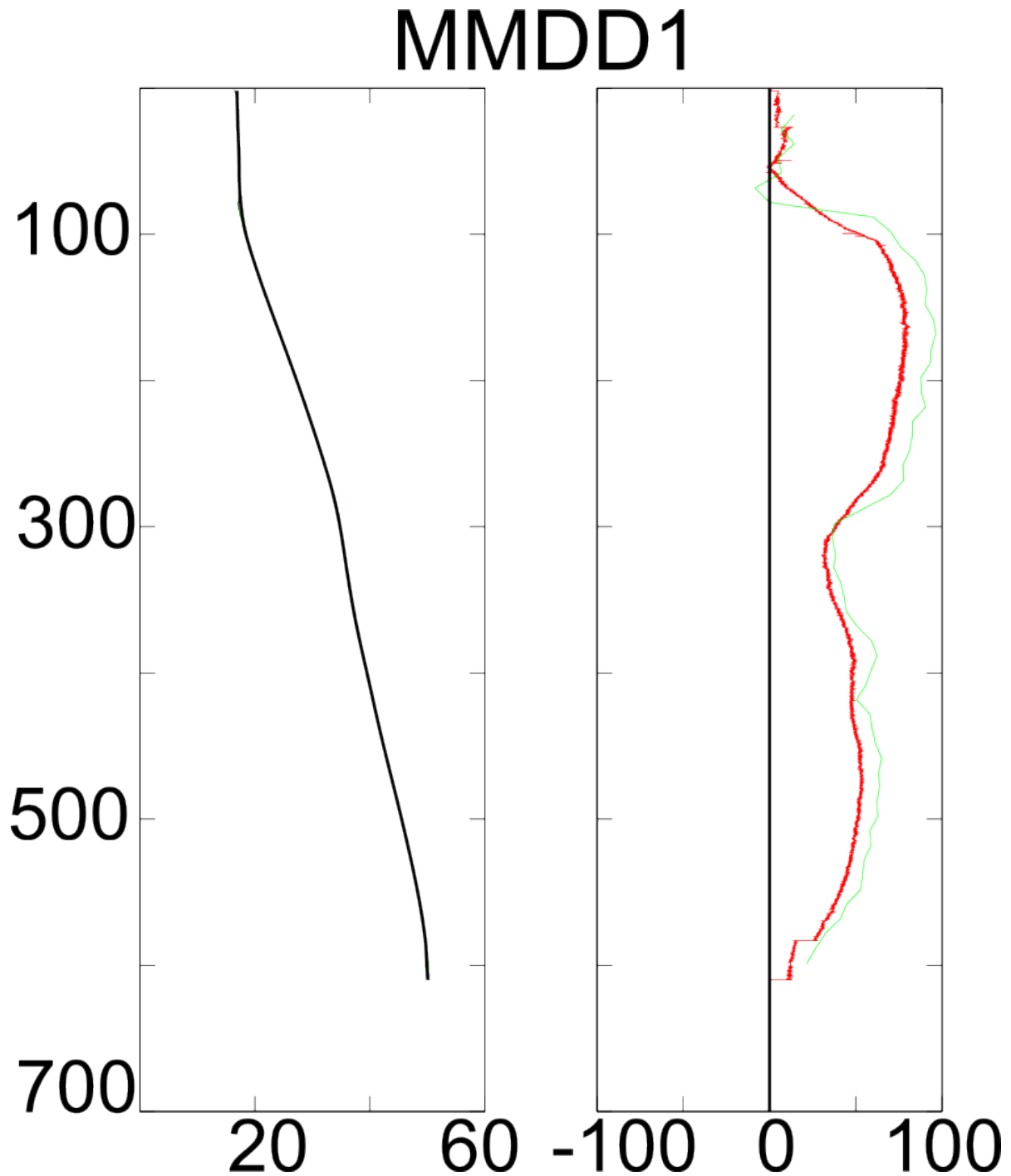
Figure 5: An analysis of thermal variations with depth, within drillhole MMDD1. Subplots include (a) temperature, (b) thermal gradient and (c) reduced temperature. The original data has also been supplemented with a moving mean and a weighted mean. 620 m was the deepest the hole was surveyed due to the wireline reaching end limit.

psammite with foliations. The lithologies resulted in a harmonic mean of 3.0398 ± 0.0212.
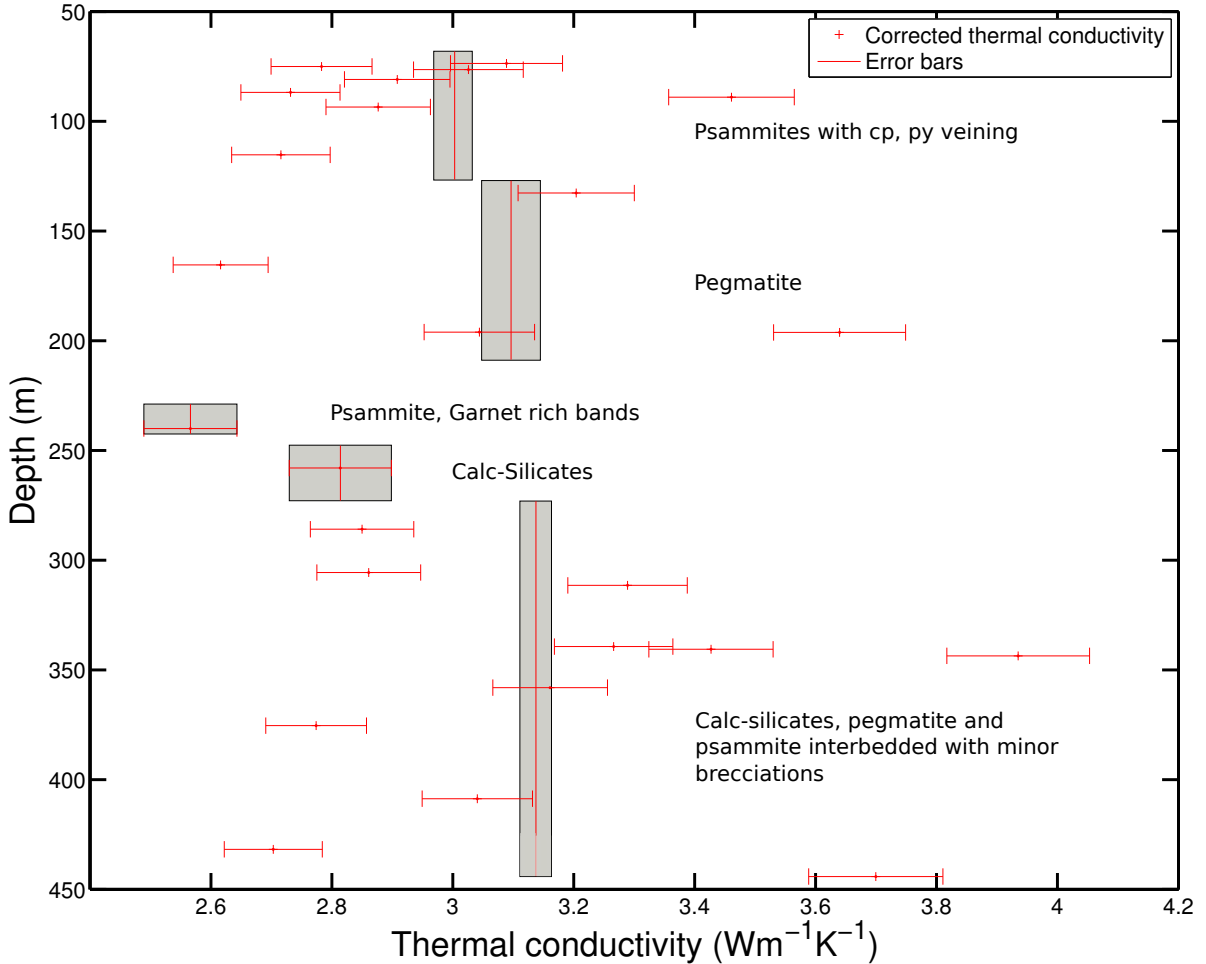
Figure 6: Thermal conductivity of the lithologies of 14DDCT001. The data points have an associated error which has been calculated through error propagation, with the vertical line being the harmonic mean of the thermal conductivity of that given lithology.

The thermal conductivity across the three lithologies of drillhole CHDCu01 is seen in Figure 7. The granite lithology has a range of thermal conductivities from 2.351 to 2.820 $\mathrm{Wm^{-1}K^{-1}}$ (once rejecting one measurement at 3.9 $\mathrm{Wm^{-1}K^{-1}}$ as it is greater than three standard deviations away from the mean) with a harmonic mean of 3.043 $\mathrm{Wm^{-1}K^{-1}}$. The garnet-magnetite gneiss has a harmonic mean of 2.575 $\mathrm{Wm^{-1}K^{-1}}$ and a range from 2.4 to 3 $\mathrm{Wm^{-1}K^{-1}}$. The deepest lithology of drillhole CHDCu01 contains the interbedded

gneiss with qtz and K-feld. This has a harmonic mean of 2.351 $Wm^{-1}K^{-1}$ and a range from 1.85 to 3 $Wm^{-1}K^{-1}$.
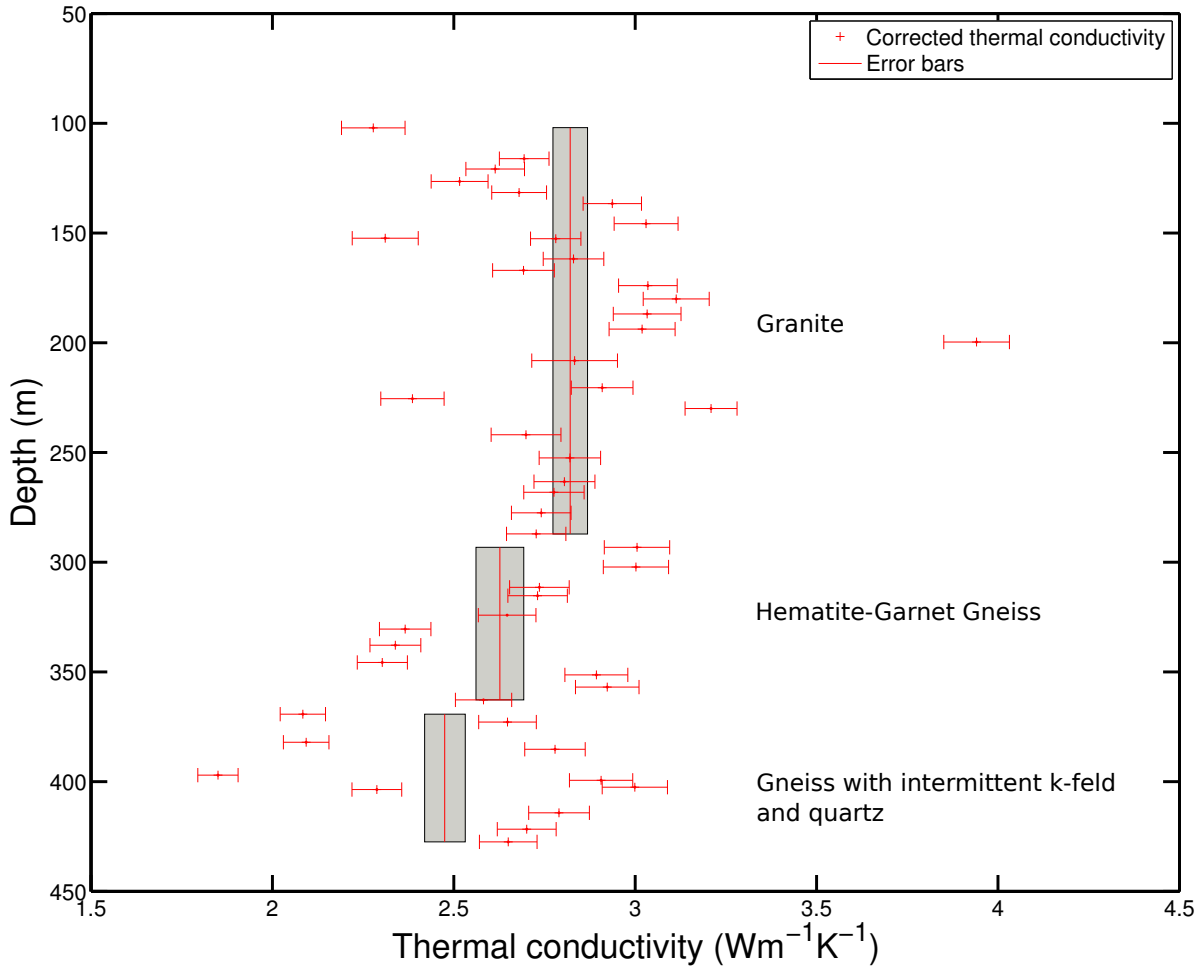
Figure 7: Thermal conductivity of the lithologies of CHDCu01. The data points have an associated error which has been calculated through error propagation. The vertical line within each lithological rectangle is the harmonic mean of the thermal conductivity of that given lithology

The four intervals of GP004D (Figure 8) have a range from 2.6995 to 3.2539 $Wm^{-1}K^{-1}$, with *2* having the greatest conductivity at $3.254 \pm 0.160 Wm^{-1}K^{-1}$ and *4*, the lowest at $2.700 \pm 0.208 Wm^{-1}K^{-1}$

The thermal conductivity of drillhole MMDD1 (Figure 9) shows greater variability and dependence on individual lithologies. The Whyalla Sandstone has a harmonic mean
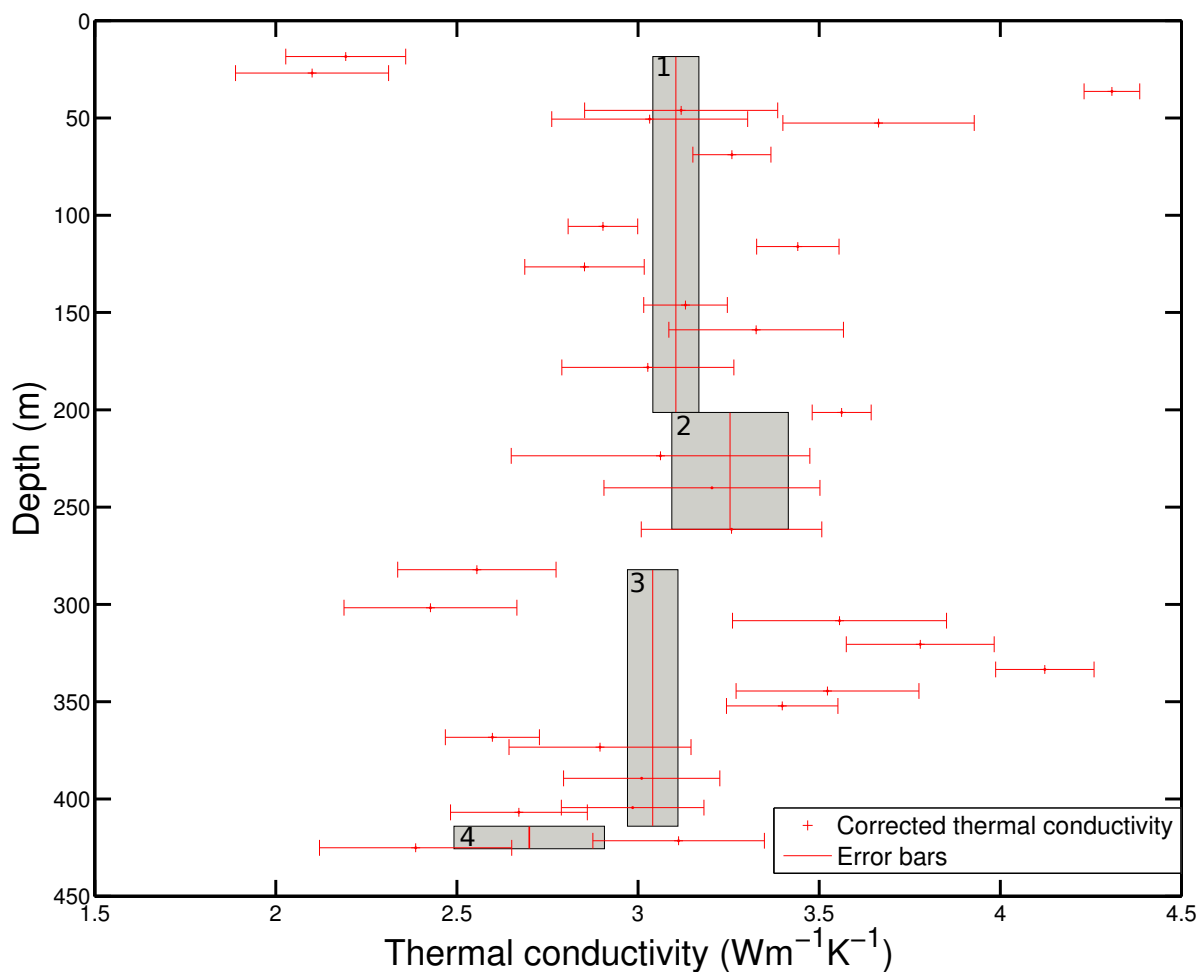
Figure 8: The four intervals of GP004D. As stated previously this hole contained no lithological data and hence intervals were determined by temperature and depth data.

of $3.743 \pm 0.150 \mathrm{Wm^{-1}K^{-1}}$ which is the largest of the four lithologies. Additionally the Beda Volcanics are contrary to what is expected given the geological terrane. Even with such a large thermal conductivity for a given lithology, harmonic mean of MMDD1 is $2.753 \pm 0.0041 \mathrm{Wm^{-1}K^{-1}}$
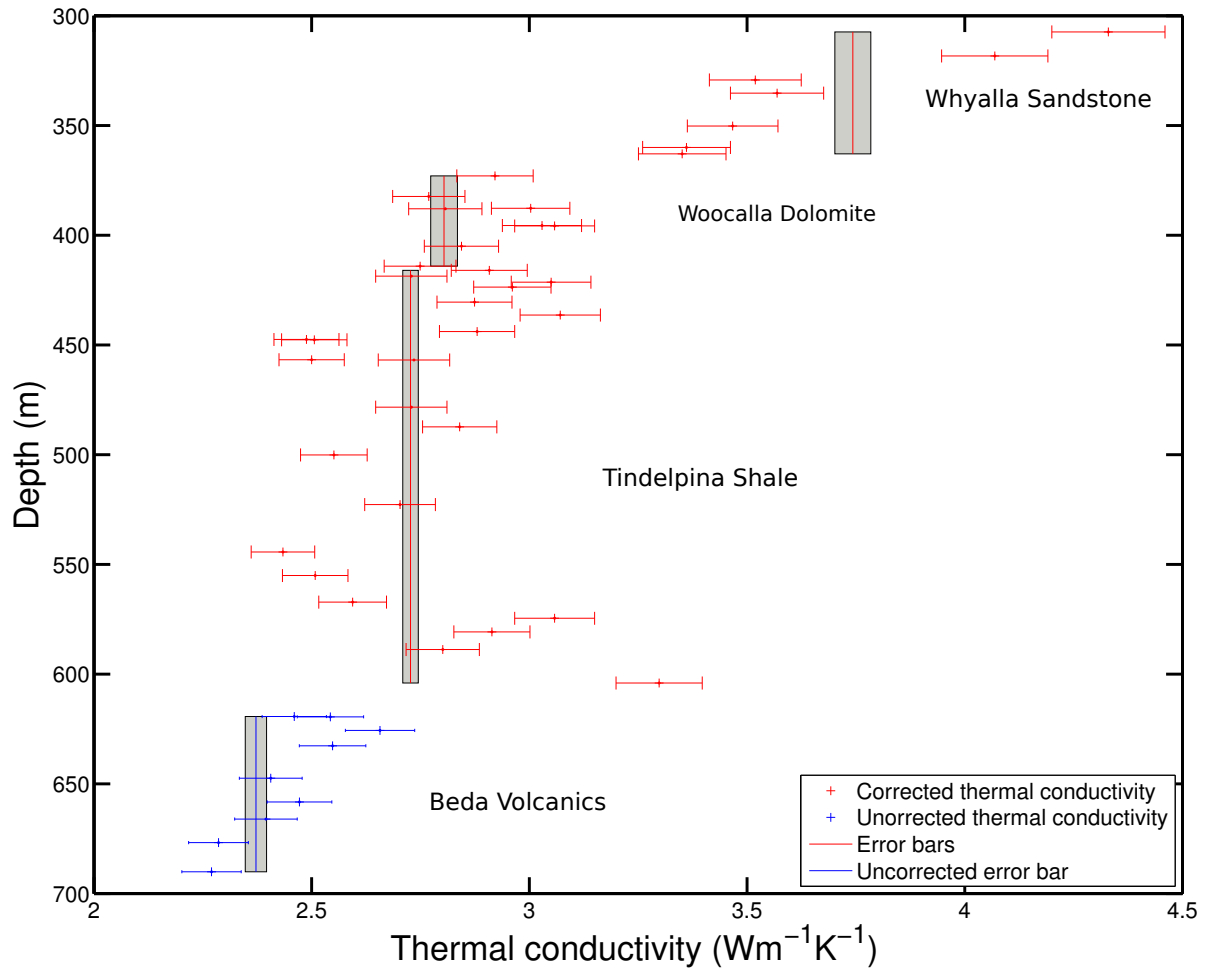
Figure 9: Thermal conductivity of the lithologies of MMDD1. The data points have an associated error which has been calculated through error propagation. The vertical line within each lithological rectangle is the harmonic mean of the thermal conductivity of that given lithology. MMDD1 lacked temperature data below 610 metre; therefore, the error associated with temperature was not possible to calculate. Also the harmonic mean for the Beda Volcanics as well as heat flow was unable to be determined.

Table 4: Drillhole descriptions. Includes name, coordinates, elevation, thickness of unit, thermal conductivity of interval and thermal conductivity of entire drillhole.

Drillhole	Latitude	Longitude	Elevation(m)	$\Delta h(m)$	k_i (Wm^{-1}K^{-1})	k (Wm^{-1}K^{-1})
14DDCT001	-31.989	140.74681	159	387.3 (68.1 - 455.4)		3.0398 ± 0.0212
Psammite with pyrite				58.7 (68.1 - 126.8)	3.0003 ± 0.0318	
and chalcopyrite veining						
Pegmatite				81.9 (127 - 208.9)	3.0963 ± 0.0486	
Psammite with				19.9 (209 - 228.9)	2.5660 ± 0.0770	
garnet rich bands						
Calc-silicate				25.3 (247.6 - 272.9)	2.8140 ± 0.0844	
Calc-silicate psammite				182.5 (273 - 455.4)	3.1425 ± 0.0298	
CHDCu01	-29.29011	135.120	143.10	327.9 (102.1 - 430)		2.7598 ± 0.0352
Granite				185.4 (102.1 - 287.5)	2.8197 ± 0.0477	
Hematite-Garnet Gneiss				73.4 (287.5 - 360.9)	2.6495 ± 0.0659	

Continued on next page

23

Table 4 – *Continued from previous page*

Drillhole	Latitude	Longitude	Elevation(m)	Δh(m)	$\mathbf{k_i(Wm^{-1}K^{-1})}$	$\mathbf{k_t(Wm^{-1}K^{-1})}$
Gneiss with intermittent				69.1 (360.9 - 430)	2.3510 ± 0.0560	
k-feld and qtz						
GPD004	-30.6938	134.5305	165.43	357.5 (68.1 - 425.6)		2.7736 ± 0.0790
1				182.9 (18.46 - 201.38)	3.1044 ± 0.0636	
2				60.07 (201.83 - 261.9)	3.2539 ± 0.1609	
3				131.8 (261.9 - 414)	3.0405 ± 0.0698	
4				11.6 (414 - 425.6)	2.6995 ± 0.2077	
MMDD1	-31.569	137.563	211	628.4 (61.8 - 690.2)		2.753 ± 0.0481
Whyalla Sandstone				61.8 (307.2 - 369)	3.7430 ± 0.1499	
Woocalla Dolomite				48 (369 - 417)	2.8040 ± 0.0889	
Tindelpina Shale				160 (417 - 577)	2.7270 ± 0.0493	
Beda Volcanics				113.2 (577 - 690.2)	2.3720 ± 0.0597	

Saturated versus unsaturated

The relationship between saturated and unsaturated samples was ascertained to discover the implications of thermal conductivity when core is not saturated. Figure 11 illustrates the relationship between these two variables for each drillhole. The general trend throughout all four drillhole was that the saturated thermal conductivity was greater for a given sample. The equations of the linear regressions from (a) to (d) all maintain this relationship. Another relationship that was analysed was the differing inhomogeneity between saturated and unsaturated samples. The inhomogeneity factor is an expression of variability within a sample and is given as a percentage. Figure 10 illustrates the relationship between these variables where it is seen that the unsaturated samples garner greater inhomogeneity values, and therefore a greater variability throughout a sample.

Heat flow

The product method has been used extensively throughout previous studies to obtain surface heat flow (e.g. Chaturvedi & Lory, 1980; Lam et al., 1982; Matthews, 2009). Figure 12 is a graphical representation of the differences between the heat flows of the four drillhole. The largest surface heat flow acquired was from MMDD1 with a value of 153.259 ± 14.62 mWm^{-2} (Figure 12d). The lowest acquired was from GP004D with an average of 52 ± 3.101 mWm^{-2} (Figure 12a), whilst drillhole CHDCu01 and 14DDCT001 have an average of 88.08 ± 5.7 mWm^{-2} and 100.189 ± 6.97 mWm^{-2} respectively.

A second method was used to calculate the average heat flow to supplement the product method. The Bullard method (Bullard, 1939) uses a linear relationship of thermal resistance as a function of depth to determine heat flow over an interval with a pre determined thermal gradient (Figure (13)). This method provided results for
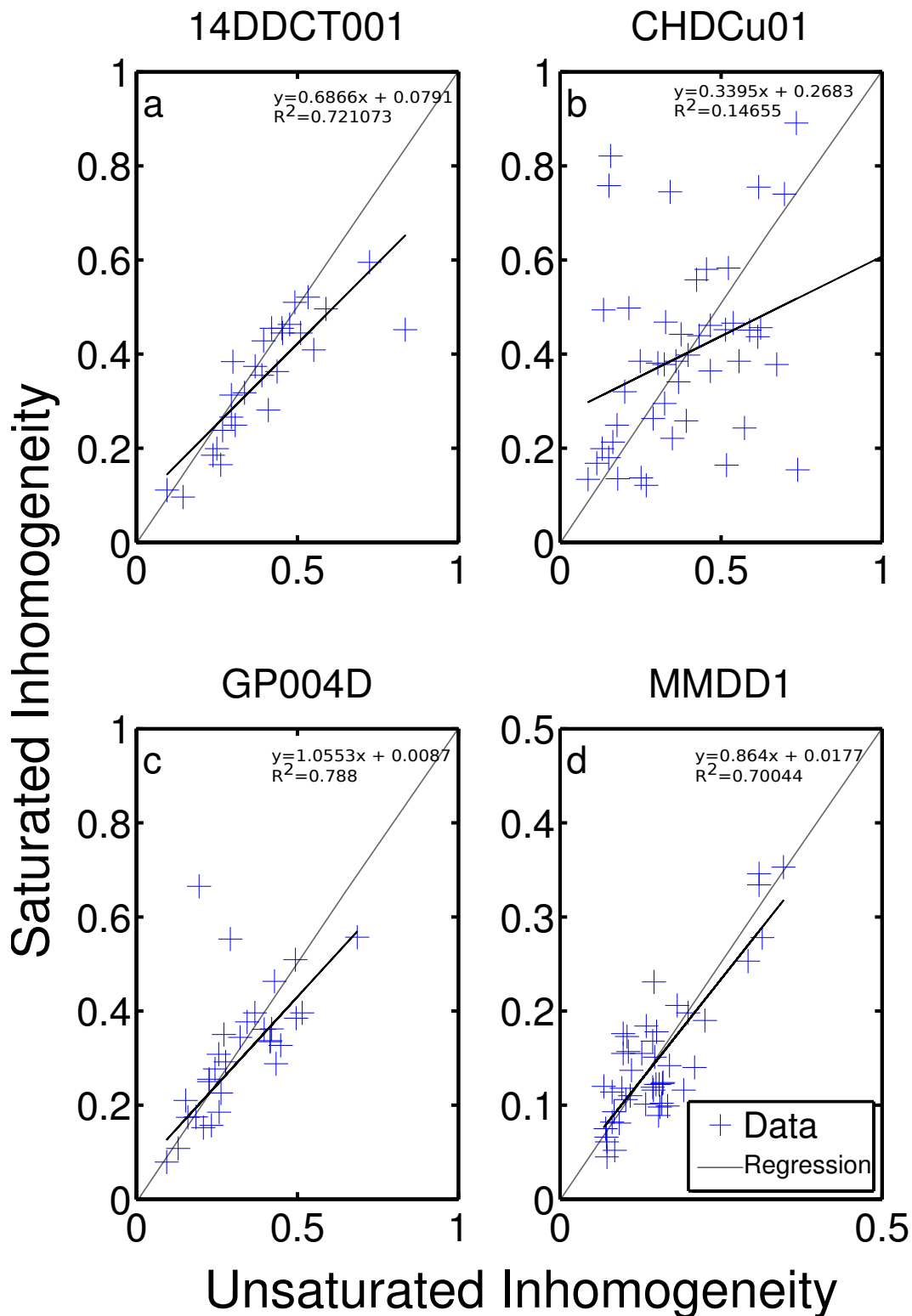
Figure 10: Relationship between the inhomogeneity of the saturated and unsaturated samples of all four drillhole. (a) 14DDCT001 (b), CHDCu01 (c), GP004D, and (d) MMDD1. For (c) outliers were present and were omitted when calculating correlation. Note that (d) has smaller x and y axis.
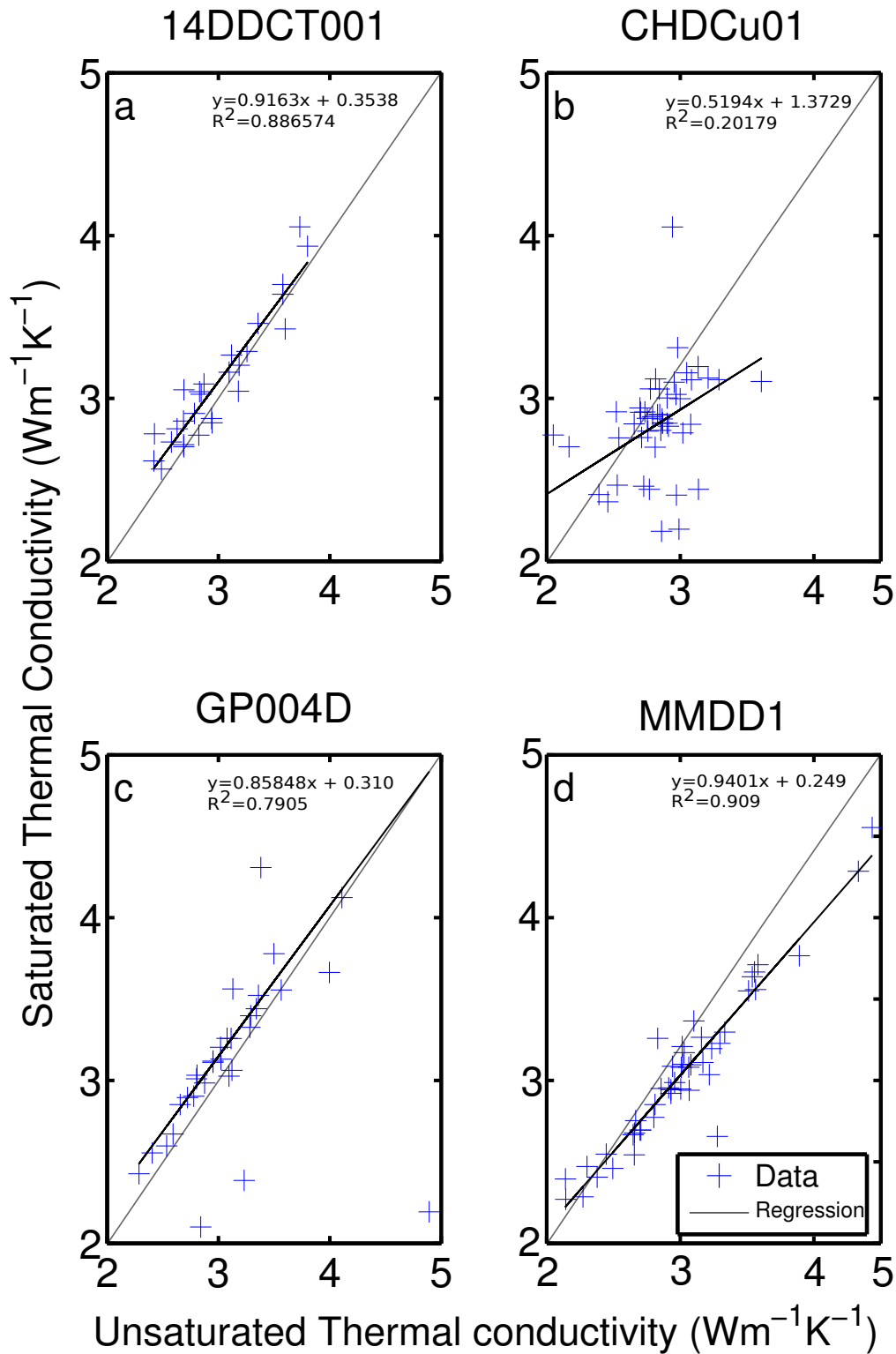
Figure 11: Relationship between the thermal conductivity of the saturated and unsaturated samples of all four drillhole. (a) 14DDCT001 (b), CHDCu01 (c), GP004D, and (d) MMDD1. For (c) outliers were present and were omitted when calculating correlation.

drillhole 14DDCT001 (Figure 13a) of 94.93 mWm $^{-2}$, CHDCu01 (Figure 13b) 91.57 mKWm^{-2}, GP004D 54.2 mKm^{-2} (Figure 13c) and an average heat flow measurement for MMDD1 (Figure 13d) of 152.2 mWm^{-2}.
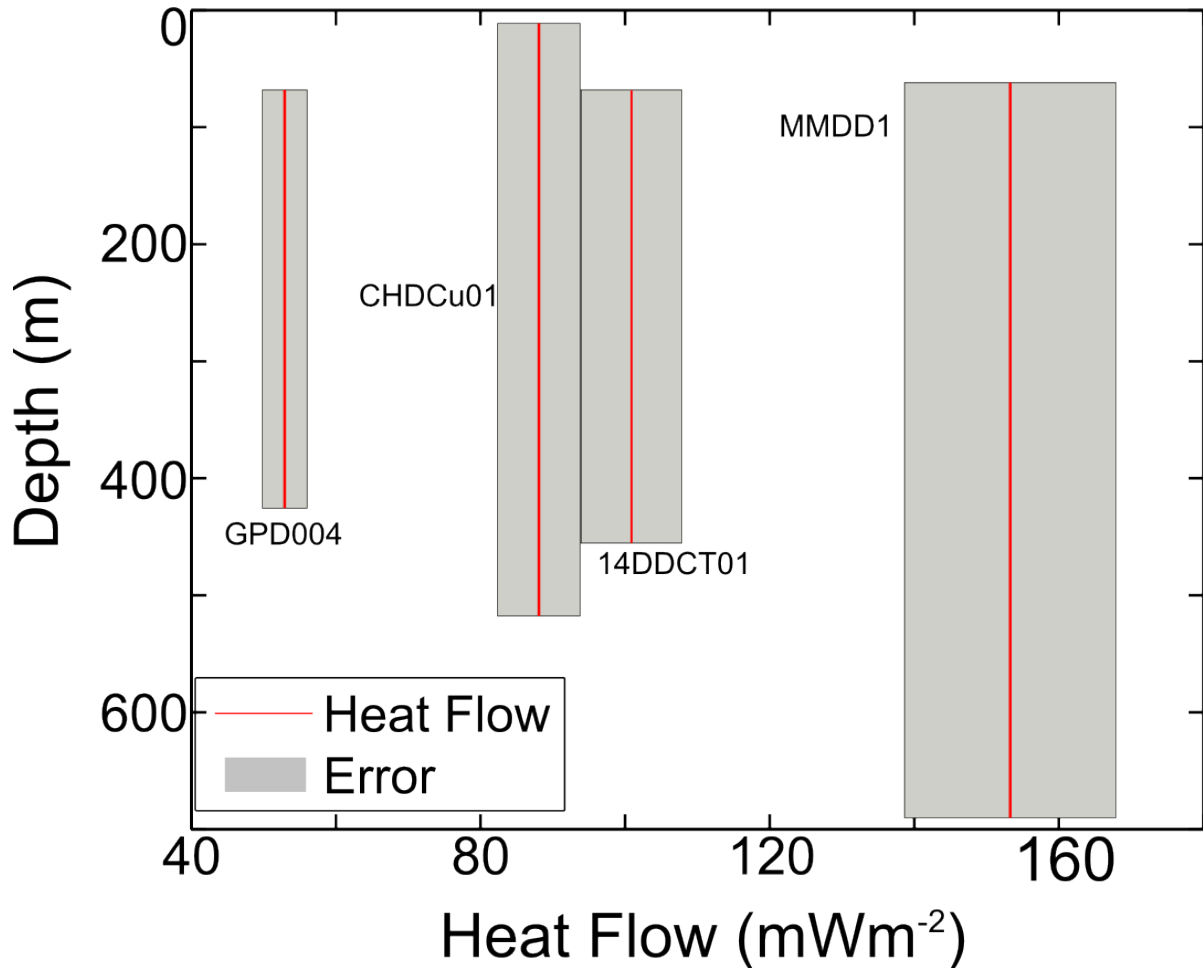
Figure 12: Heat flow of all four drillhole each with their respective heat flow values. MMDD1 has the greatest heat flow 153.259 $\pm$ 14.62 mWm^{-2}, while GPD004 has the lowest heat flow 52 $\pm$ 3.101 mWm $^{-2}$.
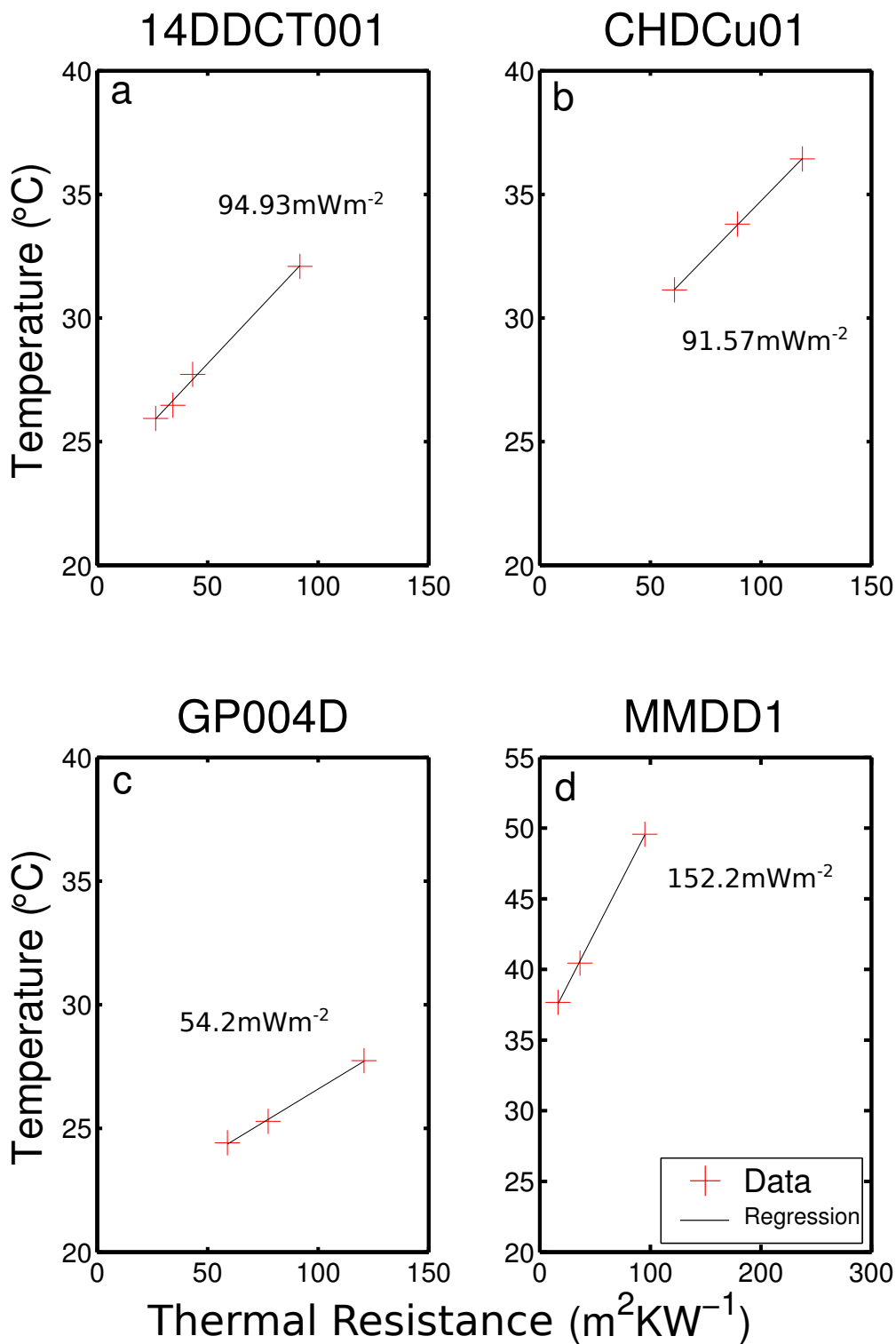
Figure 13: Bullard Plot of all four drillhole (a) 14DDCT001, (b) CHDCu01 (c) GP004D, and (d) MMDD1. Each with their respective heat flow values. Note that (d) has a greater x and y axis.

DISCUSSION

Interpretation of results

THERMAL CONDUCTIVITY

The change of thermal conductivity with temperature depends on various factors. These include opacity, composition and the shape, size of crystals. Lee & Deming (1998) found via experimentation, thermal conductivities of rocks which were less than 2.0 $Wm^{-1}K^{-1}$ at room temperature increased with increasing temperature. Thermal conductivities greater than 2.0 $Wm^{-1}K^{-1}$ at room temperature decreased with increasing temperature. Various examples of varying rock type that behave in such a manner have been documented by various authors (Birch & Clark, 1940; Cermak & Rybach, 1982; Sugawara & Yoshizawa, 1961).

Lithologies are seen to affect the thermal conductivity across all four drillhole (Figure 6 to 9). The Whyalla Sandstone of drillhole MMDD1 (Figure 9) has the lithological greatest thermal conductivity out of all four drillholes. Sandstones are abundant in quartz which has a high thermal conductivity of 7.03 $Wm^{-1}K^{-1}$ (Hofer & Shiling, 2002). Coupled with the saturation of the sample this would be a likely reasoning for the high thermal conductivity. The Beda Volcanics of the same drillhole had the second lowest thermal conductivity, 2.3720 ± 0.0597 $Wm^{-1}K^{-1}$. This volcanic sequence was vesicular and when the surface of the sample was scanned, air was too. The low thermal conductivity reading for the Beda Volcanics is likely due to the low thermal conductivity of air. Drillhole GP004D (Figure 8) had no lithological data available. The temperature and depth data was used to determine intervals (Figure 4a). Points of inflection on (a) were extrapolated to find corresponding depth. From Figure 8, the thermal conductivities somewhat match with the harmonic means barring two outliers at depths affected by

climatic conditions.

Figure 11 also illustrates the affect of saturated and unsaturated thermal conductivity against lithology. Drillhole 14DDCT001 (Figure 11a) has a correlation greater than the 1:1 line which shows that the saturated thermal conductivity is greater than unsaturated, which is good as the thermal conductivity of water is greater than the thermal conductivity of air. 14DDCT001 is a psammite drillhole and hence pore space is present for water to infiltrate. Drillhole CHDCu01 (Figure 11b) shows an uncorrelated relationship. The drillhole is composed of granites and a correlation would not generally be expected as igneous rocks have little to no pore space. MMDD1 (Figure 11d) illustrates a correlation just below the 1:1 line, which informs that the unsaturated thermal conductivity has a greater thermal conductivity than saturated. The lithologies that make up this drillhole are sandstones, dolomites and volcanics. The volcanics, due to their vesiculates are not able to saturate adequately and hence air is measured instead.

Inhomogeneity on conductivity measurements is a measure of variability within a single core sample. Figure 10 shows the inhomogeneities for each hole with respect to unsaturated and saturated conditions. This result shows that the inhomogeneity is corresponds to the lithology of the samples. Drillhole 14DDCT001 (Figure 10a) shows a marginally less correlation than compared with Figure 11a. As 14DDCT001 is a sedimentary drillhole, the saturation process opened up pore space which caused a greater void space. A greater void space garners more air (thermal conductivity of ~ 0.025 $Wm^{-1}K^{-1}$ (Balandin et al., 2008)), which in effect causes a greater inhomogeneity. Drillhole CHDCu01 (Figure 10b) corresponds with what is occuring in Figure 11b, as little correlation between variables is present. The weak foliations of the granite causes a changing composition being scanned, inducing a variability. Drillhole MMDD1 (Figure

31

10d) illustrates a portion greater than the 1:1 line which then dips underneath the line. The first stratigraphy package of MMDD1 is a sandstone causing this effect. As sandstone has a greater percentage of pore space, relative to the other lithologies, it goes through a higher degree of saturation. This saturation may not be consistent through out the whole sample and hence there will be areas of high volume of water and then areas without. This will cause a greater inhomogeneity in saturated samples compared to unsaturated.

Saturated samples differ in properties to unsaturated samples. These unsaturated samples, interestingly, differed by a significant degree in their respective inhomogeneity factors. Studies undertaken by Schlumberger Ltd. with the assistance of Chekhonin et al. (2012) concluded that the inhomogeneity of saturated samples was greater than ~15%. Unsaturated samples varied between ~4% to ~50% . In this study there was a greater range in the inhomogeneity of saturated and unsaturated samples (Figure 11). This may be due to the sampling method that was implemented by Chekhonin et al. (2012), as multiple thermal conductivity measurements were taken consecutively to reduce error on each sample.

CORRECTIONS

The temperature correction (Equation 5) from Section Methods: Corrections, was enforced with one assumption adopted; that the porosity of the samples were zero. This assumption held due to the low interconnected porosity readings which were obtained across the four drillhole, 1.4 % (see Appendix D). Chapman et al. (1984) conducted an experiment to observe how a given porosity would affect the thermal conductivity. They concluded that for a thermal conductivity range of 1.5 to 3.5 $Wm^{-1}K^{-1}$, a porosity of 10% adjusts the measured conductivity by 9 to 16%. As the greatest average interconnected porosity obtained was 12.8% (see Appendix D) this would only have a

negligible effect on the resultant thermal conductivity value. Several studies have employed the Chapman et al. (1984) correction (Deming & Chapman, 1988a; Deming & Chapman, 1988b; Correia & Fricker, 1990; Huang & Williamson, 1997).

HEAT FLOW

The values of heat flow acquired ranged from 52.926 ± 3.102 mWm^{-2} through to a high of 153.259 ± 14.62 mWm^{-2} for drillholes GP004D and MMDD1 respectively. In respect to all drillholes, GP004D had a significantly lower heat flow and is currently outside the western extent of the SAHFA (Figure 1). CHDCu01 is $\sim$50 km outside the western extent of the SAHFA, however has an anomalous heat flow value of 88.08 ± 5.7 mWm^{-2}. MMDD1 and 14DDCT01 (100.189 ± 6.97 mWm^{-2}) are both in the extent of the SAHFA and exhibit anomalously high heat flow. 14DD001 is situated in near proximity to the Willyama Inlier (Neumann et al., 2000) which has an anomalously high heat flow average of 75 mWm^{-2}. Previously mentioned CHDCu01 has an anomalously high heat flow of 88.089 ± 5.7 mWm^{-2} which changes the current extent of the SAHFA marginally to the west and constrains between GP004D.

Variations in heat flow can be observed by the non-linearity within the Bullard plots (Figure 13). High heat generation will result in a decreased heat flow, however ore grade heat producing rocks would have to be required as examined by Beardsmore (1996). Fluid movement and migration also has an adverse effect on thermal conductivity, resulting in abrupt and sustained changes in vertical heat flow. Drillhole GP004D (Figure 4a) could possibly show the effects of fluid migration at a depth from $\sim$200 to $\sim$235 m, which exhibits a decreasing thermal gradient. Another possibility for a decreasing thermal gradient is an abundance of quartz. Quartz will also induce a vertical or decreased thermal gradient.

The updated heat flow map of Australia (Figure 14) illustrates the confidence and bounds that the four heat flow determinations achieved. Figure14b, drillhole GP004D which had a heat flow of 52 ± 3.101 mWm^{-2} was also in an area with average Proterozoic lithospher heat flow. As such, confidence was added to this area of the map. CHDCu01 had a heat flow of 88.08 ± 5.7 mWm^{-2} and was located in an area of relative spareness (Figure 14a). This added confidence to interpolation as the previous heat flow gradient was ~ 70 mWm^{-2}, whereas now it is ~ 85 mWm^{-2}. Drillhole MMDD1 had the greatest heat flow value of 153.259 ± 14.62 mWm^{-2} and was located in an area that was previously relatively high as well. This data point did not provide much more detail to the updated heat flow map (Figure 14b), but did add confidence. Drillhole 14DDCT01 had a value of 100.189 ± 6.97 mWm^{-2} where previously that location had a heat flow of ~ 70 mWm^{-2} compared to ~ 100 mWm^{-2}.

Sources for anomalous heat flow

SAHFA is a high heat flow area ~ 40 mWm^{-2} greater than expected for terrane of similar age. Possible causes of this anomaly are:

BIAS

Potential errors associated with collecting data contribute to errors in the calculated surface heat flow. The condition of the drillhole and the physical environment to which it is exposed also dwells on the quality of the heat flow measurement. Cull (1982) has evaluated sources of potential errors and concluded that 75% of the Australian heat flow data were of 'good' quality, denoting that variables including; drillhole condition, measurements of thermal conductivity and thermal gradient were taken in a suffice manner. However there is no such reason as to why systematic and random errors from methodological techniques be sensitive to geological characteristics.

RECENT TECTONIC AND MAGMATIC ACTIVITY

Short temporal, thermal pulses give rise to increased heat flow measurements which can be associated with recent tectonic or magmatic activity (McLaren et al., 2003). Tectonic activity in the region of the SAHFA has been inactive since the Rodinia breakup $\sim$750 Ma (Myers et al., 1996). There has been some reactivation associated with the formation of the Flinders Ranges in South Australia (Sandiford, 2003) and consistent faulting in the Quaternary (Quigley et al., 2006). This leaves a vast majority of the SAHFA tectonically inactive, from major events, for the last several hundred million years.

Frictional heating due to faults can also increase heat flow (Beardsmore & Cull, 2011). When a fault occurs as continuous creep, friction is dissipated into the surrounding rock in a localised and short lived manner. Fulton (2013) studied the Tohoku-Oki fault which was responsible for moment magnitude 9.0 earthquake off Japan's coast. Two boreholes drilled $\sim$30 m and studied where temporal, thermal pulses were observed however temporal.

HIGH BASAL HEAT FLOW AND/OR UPPER CRUSTAL RADIOGENICS

Surface heat flow, q_s, is the summation of heat flow into the base of the lithosphere, q_b and the heat produced within the lithosphere from mainly radiogenic elements, q_A. Conservation of energy dictates that either, $q_b < q_A$, $q_b > q_A$ or $q_b = q_A$.

Seismic evidence for the presence of relatively cool mantle together with the lack of evidence for neotectonic processes would indicate anomalous, crustal sourced, heat flow (McLaren et al., 2003). This is supported by a compilation of more than 6000 analyses from 455 granite, gneiss and volcanic samples. At the time of felsic magmatism (1850 - 1500 Ma) that created the basement of the SAHFA, heat production rates were 25-30%

greater than the present day, such that the total component of U, Th, K contributed as much as 80 mWm^{-2} (Neumann et al., 2000). This enrichment has played a key role in the tectothermal evolution of the Proterozoic crust.

Drillholes in this study were compared to that of pre-existing heat flow data to determine depth source (Figure14). Studies by Decker (1995) in the southern Rocky Mountains and Wyoming Basin, Colorado, concluded that heat flow over relatively short ($<$60 km) distances imply crustal sources. 14DDCT001 is located within close proximity of the Willyama Inlier and due to a vast, high change in heat flow a shallow crustal source is indicative. Studies by Reiter (2007) within the San Juan Volcanic Field in southwestern Colorado, also conluded that heat flow changes over great ($>$100 km) distances suggest mantle derived sources.

MMDD1, with the highest heat flow value of 153.259 ± 14.62 mWm^{-2}, is located $\sim$100 km south of the Olympic Dam province (Hand et al., 2007). This high value is three times greater than the average for Proterozoic terranes, however given its proximity to this province, not an unrealistic determination. Even though the heat flow change was at the lower limit suggested by Reiter (2007) to be of a mantle derived source, MMDD1 would still help indicate a shallow crustal source due to the enormity of the value.
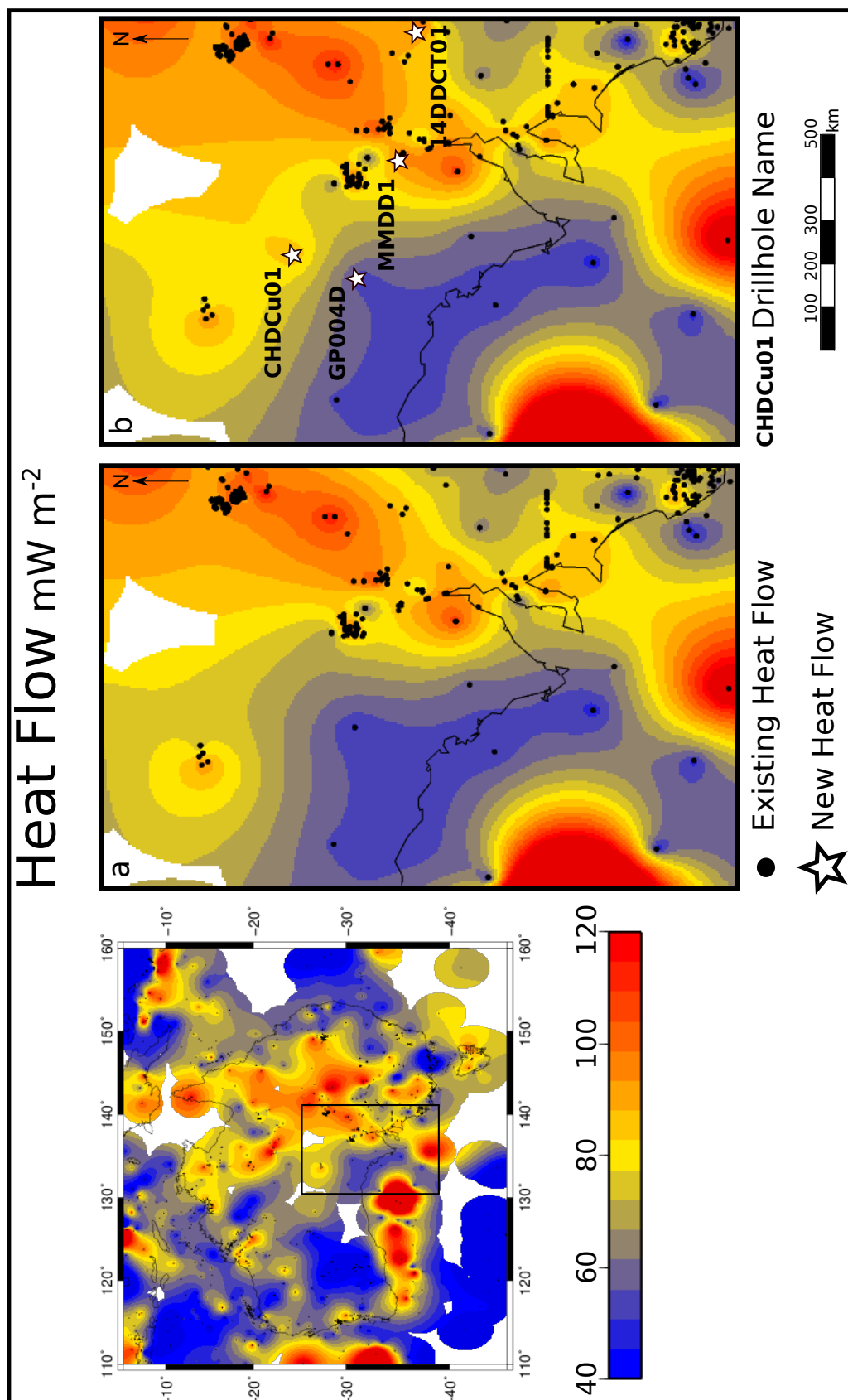
Figure 14: Heat flow map of Australia. The pre existing datset (D. Hasterok pers. comm. 2014) (a), is shown against the same dataset with the addition of new heat flow determinants from this study. (a) and (b) are both scaled with the same scale bar. GMT was used in the manufacturing of this map (Wessel et al., 2013).

CONCLUSIONS

Based on research and our thermal analyses of four drillholes that traversed the South Australian Heat Flow Anomaly (SAHFA), the following conclusions were postulated:

- Heat flow in the SAHFA is anomalously higher than other Proterozoic terranes.

- Spatial extent is/will be become better defined with each new heat flow determination. With the addition of four new heat flow values the SAHFA has become further geographically constrained, in particularly in the west. Confidence in past determinations has also been supplemented with the additional data and gradients within the extent becoming greater.

- The most probable cause of the SAHFA is due to a crustal radiogenic source. Literature and seismic data support short wave lateral change, which is indicative of crustal source. Radiogenic elements are also enriched in the upper crust, such that previously U, Th and K contributed as much as 80 mWm^{-2}.

ACKNOWLEDGEMENTS

REFERENCES

Balandin, A., Ghosh, S., Bao, W., Calizo, I., Teweldebrhan, D., Miao, F. & Lau, C. N. (2008). Superior thermal conductivity of single-layer graphene, *Nano Letters* **8**: 902–907.

Beardsmore, G. (1996). *The thermal history of the Browse Basin and it's implications for petroleum exploration*, PhD thesis, Monash University, Victoria, Australia.

Beardsmore, G. & Cull, J. (2011). *Crustal Heat Flow: a guide to measurement and modelling*, Cambridge University Press, Cambridge.

Birch, F. & Clark, H. (1940). The thermal conductivity of rocks and its dependence upon temperature and composition, *American Journal of Science* **238**: 529–558.

Bowker, C. (2013). *TCS Optical Scanner: standard operating procedure*, South Australian Centre for Geothermal Energy Research.

Bullard, E. (1939). Heat flow in South Africa, *Proceedings of the Royal Society of London. Series A, Mathematical and Physical Sciences* **173**: 474–502.

Carvalho, H. & Vacquier, V. (1977). Method for determining terrerstrial heat flow in oil fields, *Geophysics* **42**: 584–593.

Cermak, V. & Rybach, L. (1982). Thermal conductivity and specific heat of minerals and rocks, *Physical Properties of Rocks* **1-a**: 305–403.

Chapman, D. & Furlong, K. (1977). Continental heat flow - age relationships, *EOS* (58): 1240.

Chapman, D., Keho, T., Bauer, M. & Pacard, M. (1984). Heat flow in the Uinta Basin determined from bottom hole temperature (BHT) data, *Geophysics* **49**(4): 453.

Chaturvedi, L. & Lory, J. (1980). A Preliminary evaluation of geothermal potential of San Juan Basin, New Mexico, using bottom hole temperatures from oil and gas wells, *Geotherm. Res. Council.* **4**: 21–24.

Chekhonin, E., Parshin, A., Pissarenko, D., Popov, Y., Romushkevich, R., Safonov, S., Spasennykh., Chertenkov, M. & Stenin, V. (2012). When rocks get hot: Thermal properties of the reservoir rocks, *Oilfield Review* **24**: 20–37.

Clifford, P., Greenhalgh, S., Houseman, G. & Graeber, F. (2008). 3-D seismic tomography of the Adelaide Fold Belt, *Geophysical Journal International* **172**: 167–186.

Correia, A., J. F. W. & Fricker, A. (1990). Terrestrial heat-flow density estimates for the Jeanne D'Arc Basin, offshore eastern Canada., *Geophysics* **55**: 1625–1633.

Cull, J. (1982). An appraisal of Australian heat-flow data, *Journal of Australian Geology & Geophysics* **7**: 11–21.

Decker, E. (1995). Thermal regimes of the Southern Rocky Mountains and Wyoming Basin in Colorado and Wyoming in the United States, *Tectonophysics* **244**: 85–106.

Deming, D. & Chapman, D. (1988a). Heat flow in the Utah-Wyoming Thrust Belt from analysis of bottom-hole temperature data measured on oil and gas well, *Journal of Geophysical Research* **93**: 13657–13672.

Deming, D. & Chapman, D. (1988b). Inversion of bottom-hole temperature data: The Pineview field, Utah-Wyoming Thrust Belt, *Geophysics* **53**: 707–720.

Fulton, P. (2013). Low coseismic friction on the Tohoku-Oki Fault determined from temperature measurements, *Science* **342**: 1214–1217.

Hand, M., Reid, A. & Jagodzinski, L. (2007). Tectonic framework and evolution of the Gawler Craton, southern Australia, *Economic Geology* **102**: 1377–1395.

Hand, M., S. M. & Wyborn, L. (1999). Some thermal consequences of high heat production in the Australian Proterozoic, *AGSO Research Newsletter* **30**.

Hofer, M. & Shiling, F. (2002). Heat transfer in quartz, orthoclase, and sanidine at elevated temperature, *Physics and Chemistry of Minerals* **29**: 571–584.

Houseman, G., Cull, J., Muir, P. & Paterson, H. (1989). Geothermal signatures and uranium ore deposits on the Stuart Shelf of South Australia., *Geophysics* **54**: 158–170.

Huang, Z. & Williamson, M. A. (1997). The thermal conductivity and heat flow density of the Jeanne d'Arc Basin, off shore eastern Canada., *Tectonophysics* **233**: 177–492.

Lam, H., F.W., J. & Lambert, C. (1982). Geothermal gradients in the Hinton area of west-central Alberta, *Canadian Journal of Earth Sciences* **19**: 755–766.

Lambert, I., McAndrew, J. & Jones, H. (1971). Geochemical and bacteriological studies of the cupriferous environment at Pernatty Lagoon., *AusIMM. Proceedings* **240**: 15–23.

Lee, Y. & Deming, D. (1998). Evaluation of thermal conductivity temperature corrections applied in terrestrial heat flow studies, *Journal of Geophysical Research* **103**: 2447–2453.

Matthews, C. (2009). Geothermal energy prospectivity of the Torrens Hinge Zone: evidence from new heat flow data, *Exploration Geophysics* **40**: 288 – 300.

Matthews, C. & Beardsome, G. (2007). New heat flow data from south-eastern South Australia, *Exploration Geophysics* **38**: 260–269.

McLaren, S., Sandiford, M., Hand, M., Neumann, N., Wyborn, L. & Bastrakova, I. (2003). The hot southern continent: heat flow and heat production in Australian Proterozoic terranes, *Geological Society of Australia Special Publication* **22**: 157–167.

Michaut, C. & Jaupart, C. (2009). Thermal evolution of cratonic roots, *Lithos* **109**: 47–60.

Morgan, P. (1984). The thermal structure and thermal evolution of the continental lithosphere, *Phys. Chem. Earth* (15): 107–185.

Myers, J., Shaw, R. & Tyler, I. (1996). Tectonic evolution of Proterozoic Australia, *Tectonics* **15**: 1431–1446.

Neumann, N., Sandiford, M. & Foden, J. (2000). Regional geochemistry and continental heat flow: implications for the origin of the South Australian heat flow anomaly, *Earth and Planetary Science Letters* **183**: 107–120.

Patashnik, O. (1988). BibTeX-ing. Documentation for general BibTeX users.

Pollack, H. (1986). Cratonization and thermal evolution of the mantle, *Earth Planet. Sci. Lett* **80**: 175–182.

Pollack, H., Hurter, S. & Johnson, J. (1993). Heat flow from the Earth's Interior: analysis of the global data set, *Reviews of Geophysics* **31**(3): 267–280.

Popov, Y., Pribnow, D., Sass, J., Williams, C. & Burkhardt, H. (1999). Characterisation of rock thermal conductivity by high-resolution optical scanning, *Geothermics* **28**: 253–276.

Preiss, W. (2000). The Adelaide Geosyncline of South Australia and its significance in Neoproterozoic continental reconstruction, *Precambrian Research* **100**(1-3): 21–63. cited By (since 1996)227.

Preiss, W., E.M., A., W.M., C. & Schwarz, M. (2002). Towards defining South Australia's geological provinces and sedimentary basins, *MESA Journal* **27**: 39–50.

Quigley, M., Cupper, M. & Sandiford, M. (2006). Quaternary faults of south-central Australia: palaeoseismicity, slip rates and origin, *Australian Journal of Earth Sciences* **53**: 285–301.

Reiter, M. (2007). Geothermal anomalies in the crust and upper mantle along Southern Rocky Mountain transitions, *Geological Society of America* **120**: 431–441.

Robertson, R.S., a. P. W., Crooks, A., Hill, P. & Sheard, M. (1998). Review of the Proterozoic geology and mineral potential of the Curnamona Province in South Australia, *AGSO Journal of Australian Geology and Geophysics* **17**: 169–182.

Sandiford, M. (2003). Neotectonis of southeastern Australia: linking the Quaternary faulting record with seismicity and *in situ* stress, *Geological Society of Australia Special Publication* **22**: 1070–1109.

Stewart, J. & Betts, P. (2010). Late PaleoMesoproterozoic plate margin deformation in the southern Gawler Craton: insights from structural and aeromagnetic analysis, *Precambrian Research* **177**(12): 55 – 72.

Sugawara, A. & Yoshizawa, Y. (1961). An investigation on the thermal conductivity of porous materials and its application to porous rock, *Australian Journal of Physics* **14**: 469–480.

Thakur, M. & Blackwell, D. (2006). Heat flow in the Archean cratons: new facts and Insights into lithospheric thickness and distribution of radioactive elements, *AGU Fall Meeting Abstracts* p. 628.

Webb, A. & Horr, G. (1978). The RB-Sr age and petrology of a flow from the Beda Volcanics, *Geological Survey of South Australia, Quarterly Geological Notes* **66**: 10–13.

Wessel, P., Smith, W., Scharroo, R., Luis, J. & Wobbe, F. (2013). Generic Mapping Tools: improved version releases, *EOS Trans. AGU* **94**: 409–410.

Williams, G. (1998). Late Neoproterozoic periglacial aeolian sand sheet, Stuart Shelf, South Australia, *Australian Journal of Earth Sciences* **45**: 733–741.

APPENDIX A: TCS OPTICAL SCANNER MANUAL

The Optical scanning method is based on scanning a sample surface with two temperature sensors in combination with a focused, mobile and continuously operated constant heat source. The heat source and sensors move with the same speed relative to the sample at a constant distance to each other. Temperature sensor 1 displays the value of the unheated or cold sample surface temperature to take relative, preliminary temperatures of the solids into account. The remaining sensor displays the values of the rise of corresponding maximum temperature along the heating line behind the source. This allows the determination of core thermal conductivity and thermal diffusivity simultaneously from one experiment. The merits of optical scanning include a varying sample size within one to 70 centimetres in length, with a precision and accuracy of 1.5% at the 95% confidence level, of thermal conductivity measurements within the range of 0.1 70.0 $Wm^{-1}K^{-1}$.

All cables were plugged in to the TCS to the power supply unit; then cables from the unit to the laptop were connected. A double check that the **DAQ** and **Stepper Cables** were plugged into **USB port 1** and **USB port 2** was then undertaken. Power to the TCS was then turned on at the wall socket, and then the power on button located at the rear of the power supply unit was switched on. A red light indicating this was successful was seen at the rear of the unit. The laptop was then opened on powered on via the on/off button located at the top right-hand corner of the keyboard. A screen prompting a university log in and password appeared which was then apprised with the appropriate details. Once the Windows Explorer start up screen had loaded the shortcut icon **TCS** was selected. The location of the icon was within the second column, second from the top.

Standard 1 and Standard 2. The window was closed which prompted a smaller window to open stating Set recommended heat source power? **Ok** was selected which ensured that the power level for the heat source is set to the recommended level for the standards which were selected. This procedure was repeated before each subsequent measurement session. This ensured that all parameters were set correctly. Adjustment of the temperature sensors before every measurement was taken to ensure that any changes in room temperature were taken into account by the software. **Sensor Adjustment** was selected from the main toolbar via the Sensors tab. This prompted an adjust sensors window to appear. A reference standard was selected from the standards that were not going to be used in the subsequent measurement. Upon clicking **Start** in the adjust sensors window, the reference standard was placed over the **Hot** sensor. After being prompted to, the reference standard was then placed over the **Cold** sensor.

One of the two standards which were selected was placed at the beginning of the red taped section of the scanner stage. As many samples as possible were placed on the stage with the second standard being placed after the last sample. The cylindrical samples were propped up by metal core props so they were coincident with the top of the scanner stage with the black painted lines aligned with the aperture by looking underneath the

stage. If cores were halved, the fflat side was face down. Once all the preparation was completed, **Measure!** was selected from the panel on the right hand side of the opening TCS software screen on the laptop. Heat source was lit up upon this command and the chariot began to move from the beginning of the scanner to the other. Data were being recorded on the laptop simultaneously which appeared as two lines; blue representing the cold temperature measurements, red representing the hot temperature measurements. Once the chariot reached the end of the second standard, **Stop** was selected were the **Measure!** button was once found. Once the scan was stopped a prompt screen to Save the scan file was selected and was saved in an appropriate place with systematic file naming.

APPENDIX B: DRILLHOLE SAMPLES

Table 5: Weights of samples of core from drillhole CHDCU01 with depth.

Sample No.	Dry Weight (g)	Submerged (g)	Saturated (g)	Difference (g)	Depth from (m)	Depth to (m)
2073829	1503.6	929.9	1504.4	0.8	102.1	102.38
2073830	1750.6	1084	1751.1	0.5	116.11	116.46
2073831	1543.8	955.1	1544.6	0.8	120.83	121.13
2073832	1291.5	799.2	1292.2	0.7	126.5	126.75
2073833	2051.8	1272.6	2051.9	0.1	131.55	131.96
2073785	1104.2	686.2	1105.1	0.9	136.6	136.81
2073786	1855.4	1185.1	1856.1	0.7	145.79	146.3
2073787	1257.5	781	1258.5	1	152.38	152.63
2073788	1432.1	888.7	1433.4	1.3	152.6	152.87
2073789	1433	888.4	1434.1	1.1	161.79	162.06
2073790	1191.1	753.4	1143.6	-47.5	167.03	167.23
2073791	857.7	554.9	858	0.3	174	174.36
2073792	451.5	281.4	451.3	-0.2	180.06	180.26
2073793	467.4	291.7	467.9	0.5	186.9	187.1
2073794	862	597.3	860.5	-1.5	193.8	194.1
2073795	872.4	689.2	872.6	0.2	199.71	199.91
2073796	749	471	749.3	0.3	208.18	208.49
2073797	469.7	322.1	470.3	0.6	220.53	220.7
2073798	1269.5	823		-1269.5	225.53	225.79
2073799	870.2	550.3	871.4	1.2	230	230.1
2073800	1029	675.6	1029.9	0.9	241.97	242.15

Continued on next page

45

Table 5 – Continued from previous page

Sample No.	Dry Weight (g)	Submerged (g)	Saturated (g)	Difference (g)	Depth from (m)	Depth to (m)
2073801	782.2	508.3	782.5	0.3	248	248.1
2073802	939	590.1	940	1	252.5	252.67
2073803	1549.5	978.9		-1549.5	263.32	263.61
2073804	1327.6	836.3	1328.6	1	268.18	268.41
2073805	1079.5	689.3	1550	470.5	277.52	277.72
2073806	487.9	305	488.4	0.5	287.13	287.33
2073807	584.5	371.6	585.4	0.9	293.25	293.48
2073808	1565.9	984.5	1565.8	-0.1	302.21	302.49
2073809	1129.2	700.1	1129.6	0.4	311.45	311.67
2073810	1502.5	947.9	1503.2	0.7	315.28	315.56
2073811	1371.9	869.6	1371.5	-0.4	324.15	324.4
2073812	1197.1	765.7	1198.2	1.1	330.5	330.73
2073813	735.9	456.6	737	1.1	337.87	338.17
2073814	1057.8	659.1	1061.5	3.7	345.71	345.92
2073815	1357.5	851.1	1357.5	0	351.39	351.62
2073816	1315.9	831.6	1317.9	2	356.95	357.2
2073817	1576.2	1014.7	1577.1	0.9	362.79	363.06
2073818	1695.9	1076.5	1699.4	3.5	369.25	369.55
2073819	627	388.9	627.9	0.9	372.88	373.01
2073820	569.2	325.6	510.3	-58.9	382.05	382.25
2073821	781.2	524.9	782.4	1.2	385.26	385.56
2073822	1432.8	889.9	1433.5	0.7	397.03	397.3
2073823	440.4	282.3	443.4	3	399.4	399.57

Continued on next page

Table 5 – *Continued from previous page*

Sample No.	Dry Weight (g)	Submerged (g)	Saturated (g)	Difference (g)	Depth from (m)	Depth to (m)
2073824	510.3	318	511.1	0.8	402.58	402.78
2073825	617	400.7	617	0	403.6	403.82
2073826	1440.9	911	1446.1	5.2	414.23	414.5
2073827	1142.7	720.9	1144.2	1.5	421.71	421.91
2073828	793.1	501.2	794.1	1	427.49	427.63

Table 6: Weights of samples of core from drillhole MMDD1 with depth.

Sample No.	Dry Weight (g)	Submerged (g)	Saturated (g)	Difference (g)	Depth from (m)	Depth to (m)
2073785	1104.2	686.2	1105.1	0.9	136.6	136.81
2073786	1855.4	1185.1	1856.1	0.7	145.79	146.3
2073787	1257.5	781	1258.5	1	152.38	152.63
2073788	1432.1	888.7	1433.4	1.3	152.6	152.87
2073789	1433	888.4	1434.1	1.1	161.79	162.06
2073790	1191.1	753.4	1143.6	-47.5	167.03	167.23
2073791	857.7	554.9	858	0.3	174	174.36
2073792	451.5	281.4	451.3	-0.2	180.06	180.26
2073793	467.4	291.7	467.9	0.5	186.9	187.1
2073794	862	597.3	860.5	-1.5	193.8	194.1
2073795	872.4	689.2	872.6	0.2	199.71	199.91
2073796	749	471	749.3	0.3	208.18	208.49
2073797	469.7	322.1	470.3	0.6	220.53	220.7
2073798	1269.5	823		-1269.5	225.53	225.79
2073799	870.2	550.3	871.4	1.2	230	230.1
2073800	1029	675.6	1029.9	0.9	241.97	242.15
2073801	782.2	508.3	782.5	0.3	248	248.1
2073802	939	590.1	940	1	252.5	252.67
2073803	1549.5	978.9		-1549.5	263.32	263.61
2073804	1327.6	836.3	1328.6	1	268.18	268.41
2073805	1079.5	689.3	1550	470.5	277.52	277.72

Continued on next page

48

Table 6 – *Continued from previous page*

Sample No.	Dry Weight (g)	Submerged (g)	Saturated (g)	Difference (g)	Depth from (m)	Depth to (m)
2073806	487.9	305	488.4	0.5	287.13	287.33
2073807	584.5	371.6	585.4	0.9	293.25	293.48
2073808	1565.9	984.5	1565.8	-0.1	302.21	302.49
2073809	1129.2	700.1	1129.6	0.4	311.45	311.67
2073810	1502.5	947.9	1503.2	0.7	315.28	315.56
2073811	1371.9	869.6	1371.5	-0.4	324.15	324.4
2073812	1197.1	765.7	1198.2	1.1	330.5	330.73
2073813	735.9	456.6	737	1.1	337.87	338.17
2073814	1057.8	659.1	1061.5	3.7	345.71	345.92
2073815	1357.5	851.1	1357.5	0	351.39	351.62
2073816	1315.9	831.6	1317.9	2	356.95	357.2
2073817	1576.2	1014.7	1577.1	0.9	362.79	363.06
2073818	1695.9	1076.5	1699.4	3.5	369.25	369.55
2073819	627	388.9	627.9	0.9	372.88	373.01
2073820	569.2	325.6	510.3	-58.9	382.05	382.25
2073821	781.2	524.9	782.4	1.2	385.26	385.56
2073822	1432.8	889.9	1433.5	0.7	397.03	397.3
2073823	440.4	282.3	443.4	3	399.4	399.57
2073824	510.3	318	511.1	0.8	402.58	402.78
2073825	617	400.7	617	0	403.6	403.82
2073826	1440.9	911	1446.1	5.2	414.23	414.5
2073827	1142.7	720.9	1144.2	1.5	421.71	421.91
2073828	793.1	501.2	794.1	1	427.49	427.63

Continued on next page

Table 6 – *Continued from previous page*

Sample No.	Dry Weight (g)	Submerged (g)	Saturated (g)	Difference (g)	Depth from (m)	Depth to (m)
2073829	1503.6	929.9	1504.4	0.8	102.1	102.38
2073830	1750.6	1084	1751.1	0.5	116.11	116.46
2073831	1543.8	955.1	1544.6	0.8	120.83	121.13
2073832	1291.5	799.2	1292.2	0.7	126.5	126.75
2073833	2051.8	1272.6	2051.9	0.1	131.55	131.96
2073834	665.8	426.9	666.4	0.6	94.62	94.85

APPENDIX C: THERMAL CONDUCTIVITY

Table 7: Saturated thermal conductivity of MMDD1. Includes temperature corrected thermal conductivity, K_c

Sample No.	K_{mean}	K_{min}	K max	K_c	Inhomo
2073785	2.857	2.618	3.594	3.003	0.341
2073786	2.949	2.555	3.671	3.099	0.378
2073787	2.25	1.69	2.677	2.365	0.439
2073788	2.709	2.522	2.976	2.847	0.168
2073789	2.759	2.577	2.949	2.900	0.135
2073790	2.626	1.957	2.968	2.760	0.385
2073791	3.114	2.383	3.817	3.114	0.461
2073792	3.196	2.826	4.057	3.196	0.385
2073793	2.964	2.155	4.347	3.115	0.74
2073794	3.104	2.322	4.131	3.104	0.583
2073795	4.053	2.698	4.958	4.053	0.558
2073796	2.918	2.166	3.277	2.918	0.381
2073797	2.853	2.294	3.625	2.999	0.466
2073798	2.461	2.202	2.836	2.461	0.258
2073799	3.151	2.083	4.431	3.312	0.745
2073800	2.653	2.118	3.428	2.788	0.494
2073801	2.774	2.477	3.365	2.915	0.32
2073802	2.761	2.592	2.927	2.902	0.121
2073803	2.735	2.44	3.044	2.874	0.221
2073804	2.703	2.191	2.902	2.841	0.263
2073805	2.692	2.089	3.302	2.829	0.451
2073806	NO	DATA			
2073807	3.12	1.857	4.222	3.120	0.758
2073808	2.709	2.535	2.9	2.847	0.137
2073809	2.706	2.309	2.966	2.844	0.243
2073810	2.624	2.128	3.325	2.758	0.456
2073811	2.348	1.673	3.035	2.468	0.58
2073812	2.323	1.838	2.716	2.441	0.378
2073813	2.406	1.931	3.129	2.406	0.498

Continued on next page

Table 7 – *Continued from previous page*

Sample No.	K_{mean}	K_{min}	K max	K_c	Inhomo
2073814	2.878	2.507	3.357	3.025	0.295
2073815	2.91	2.508	3.629	3.058	0.385
2073816	2.572	2.334	2.73	2.703	0.154
2073817	2.078	1.63	3.141	2.184	0.727
2073818	2.641	1.975	4.145	2.776	0.821
2073819	2.09	1.919	2.262	2.197	0.164
2073820	2.917	2.047	3.442	2.917	0.478
2073821	NO	DATA			
2073822	1.852	1.663	2.032	1.946	0.199
2073823	3.058	1.877	4.188	3.058	0.755
2073824	3.157	2.561	3.942	3.157	0.437
2073825	2.41	1.971	2.847	2.410	0.364
2073826	2.799	1.966	4.459	2.942	0.891
2073827	2.712	2.244	3.512	2.850	0.468
2073828	2.663	2.305	3.483	2.799	0.442
2073829	2.323	1.838	2.716	2.441	0.398
2073830	2.748	2.546	3.04	2.888	0.18
2073831	2.668	2.388	3.593	2.804	0.452
2073832	2.569	2.404	2.748	2.700	0.134
2073833	2.738	2.56	3.143	2.878	0.213
2073834	2.974	2.634	3.373	3.126	0.249

Table 8: Saturated thermal conductivity of CHDCu01. Includes temperature corrected thermal conductivity, K_c

Sample No.	K_{mean}	K_{min}	K max	K_c	Inhomo
2073745	4.252	3.845	4.829	4.554	0.231
2073746	4.001	3.609	4.403	4.285	0.198
2073747	3.511	3.273	3.701	3.711	0.122
2073748	3.563	3.346	3.79	3.766	0.122
2073749	3.423	3.272	3.577	3.666	0.089
2073750	3.367	3.291	3.562	3.559	0.102
2073751	3.359	3.191	3.559	3.550	0.11

Continued on next page

Table 8 – *Continued from previous page*

Sample No.	K_{mean}	K_{min}	K max	K_c	Inhomo
2073752	2.894	2.443	3.409	3.099	0.334
2073753	2.784	2.519	2.952	2.943	0.155
2073754a	3.023	2.684	3.257	3.195	0.19
2073754b	2.789	2.74	2.886	2.987	0.052
2073755	3.054	2.851	3.206	3.228	0.116
2073755a	3.083	2.927	3.229	3.259	0.098
2073756	2.872	2.634	3.226	3.036	0.206
2073757	2.781	2.606	2.952	2.940	0.155
2073758a	2.943	2.721	3.216	3.111	0.168
2073758b	2.763	2.615	2.895	2.920	0.101
2073759a	3.089	2.605	3.386	3.265	0.253
2073759b	3	2.586	3.421	3.171	0.278
2073760	2.932	2.789	3.137	3.082	0.119
2073761	3.122	2.864	3.965	3.297	0.353
2073762	2.946	2.828	3.142	3.096	0.106
2073763a	2.547	2.488	2.602	2.677	0.045
2073763b	2.565	2.485	2.642	2.696	0.061
2073764a	2.564	2.482	2.692	2.695	0.082
2073764b	2.805	2.585	2.983	2.948	0.142
2073765	2.811	2.702	2.963	2.954	0.093
2073766	2.931	2.743	3.081	3.080	0.116
2073767	2.639	2.443	2.841	2.774	0.151
2073768					
2073769	2.808	2.601	3.102	2.951	0.178
2073770a	2.537	2.45	2.642	2.666	0.075
2073770b					
2073771	2.62	2.494	2.755	2.754	0.099
2073772	2.714	2.482	2.983	2.852	0.184
2073773	3.202	3.028	3.423	3.365	0.123
2073774	3.053	2.845	3.373	3.209	0.173
2073775	2.937	2.699	3.717	3.087	0.346
2073776	3.461	3.242	3.671	3.638	0.124
2073777a	2.341	2.188	2.465	2.460	0.118
2073777b	2.42	2.303	2.594	2.543	0.12

Continued on next page

Table 8 – *Continued from previous page*

Sample No.	K_{mean}	K_{min}	K max	K_c	Inhomo
2073778	2.528	2.325	2.722	2.657	0.157
2073779	2.424	2.26	2.6	2.548	0.14
2073780	2.289	2.084	2.487	2.406	0.176
2073781	2.352	2.264	2.419	2.472	0.066
2073782	2.279	2.187	2.371	2.395	0.081
2073783	2.175	2.036	2.334	2.286	0.137
2073784	2.16	2.078	2.325	2.270	0.114

APPENDIX D: POROSITY

Table 9: Porosity of 14DDCT01

Sample No.	M_{dry} (g)	M_{sat} (g)	M_{sub} (g)	V_b (cm^3)	V_p (cm^3)	ϕ
5	1183.9	1185.5	762.1	423.4	1.6000	0.0038
6	1275.9	1276.4	823.1	453.3	0.5000	0.0011
7	1660	1661.1	1059.6	601.5	1.1000	0.0018
10	1670.2	1675.4	1072.9	602.5	5.2000	0.0086
11	1649.9	1651.4	1030.2	621.2	1.5000	0.0024
18	1484.7	1486.3	966.7	519.6	1.6000	0.0031
24	1666.4	1669.6	1070.9	598.7	3.2000	0.0053
35	552.3	554.8	350.1	204.7	2.5000	0.0122
37	390.8	392	247.1	144.9	1.2000	0.0083
41	647.8	651.9	445.3	206.6	4.1000	0.0198
43	653.5	656.1	411.6	244.5	2.6000	0.0106
47	761.9	762.5	486.5	276	0.6000	0.0022
48a	244	244.5	149.7	94.8	0.5000	0.0053
48b	371.4	372	229.9	142.1	0.6000	0.0042
51	1233.2	1234	796.5	437.5	0.8000	0.0018
54	1572.1	1572.4	1020.4	552	0.3000	0.0005
56	1514.2	1516.8	978.9	537.9	2.6000	0.0048

Table 10: Porosity of CHDCu01

Sample No.	$\mathbf{M}_{dry}$ (g)	$\mathbf{M}_{sat}$ (g)	$\mathbf{M}_{sub}$ (g)	$\mathbf{V}_b$ (cm^3)	$\mathbf{V}_p$ (cm^3)	ϕ
2073785	1104.2	1105.1	686.2	418.9	0.9000	0.0021
2073786	1855.4	1856.1	1185.1	671	0.7000	0.0010
2073787	1257.5	1258.5	781	477.5	1.0000	0.0021
2073788	1432.1	1433.4	888.7	544.7	1.3000	0.0024
2073789	1433	1434.1	888.4	545.7	1.1000	0.0020
2073791	857.7	858	554.9	303.1	0.3000	0.0010
2073793	467.4	467.9	291.7	176.2	0.5000	0.0028
2073795	872.4	872.6	689.2	183.4	0.2000	0.0011
2073796	749	749.3	471	278.3	0.3000	0.0011
2073797	469.7	470.3	322.1	148.2	0.6000	0.0040
2073799	870.2	871.4	550.3	321.1	1.2000	0.0037
2073800	1029	1029.9	675.6	354.3	0.9000	0.0025
2073801	782.2	782.5	508.3	274.2	0.3000	0.0011
2073802	939	940	590.1	349.9	1.0000	0.0029
2073804	1327.6	1328.6	836.3	492.3	1.0000	0.0020
2073805	1079.5	1550	689.3	860.7	470.5000	0.5466
2073806	487.9	488.4	305	183.4	0.5000	0.0027
2073807	584.5	585.4	371.6	213.8	0.9000	0.0042
2073809	1129.2	1129.6	700.1	429.5	0.4000	0.0009
2073810	1502.5	1503.2	947.9	555.3	0.7000	0.0013
2073812	1197.1	1198.2	765.7	432.5	1.1000	0.0025
2073813	735.9	737	456.6	280.4	1.1000	0.0039
2073814	1057.8	1061.5	659.1	402.4	3.7000	0.0092
2073815	1357.5	1357.5	851.1	506.4	0.0000	0.0000
2073816	1315.9	1317.9	831.6	486.3	2.0000	0.0041
2073817	1576.2	1577.1	1014.7	562.4	0.9000	0.0016
2073818	1695.9	1699.4	1076.5	622.9	3.5000	0.0056
2073819	627	627.9	388.9	239	0.9000	0.0038
2073821	781.2	782.4	524.9	257.5	1.2000	0.0047
2073822	1432.8	1433.5	889.9	543.6	0.7000	0.0013
2073823	440.4	443.4	282.3	161.1	3.0000	0.0186
2073824	510.3	511.1	318	193.1	0.8000	0.0041

Continued on next page

Table 10 – *Continued from previous page*

Sample No.	M_{dry} (g)	M_{sat} (g)	M_{sub} (g)	V_b (cm^3)	V_p (cm^3)	ϕ
2073825	617	617	400.7	216.3	0.0000	0.0000
2073826	1440.9	1446.1	911	535.1	5.2000	0.0097
2073827	1142.7	1144.2	720.9	423.3	1.5000	0.0035
2073828	793.1	794.1	501.2	292.9	1.0000	0.0034
2073829	1503.6	1504.4	929.9	574.5	0.8000	0.0014
2073830	1750.6	1751.1	1084	667.1	0.5000	0.0007
2073831	1543.8	1544.6	955.1	589.5	0.8000	0.0014
2073832	1291.5	1292.2	799.2	493	0.7000	0.0014
2073833	2051.8	2051.9	1272.6	779.3	0.1000	0.0001
2073834	665.8	666.4	426.9	239.5	0.6000	0.0025

Table 11: Porosity of GP004D

Sample No.	M_{dry} (g)	M_{sat} (g)	M_{sub} (g)	V_b (cm^3)	V_p (cm^3)	ϕ
2067646	451.5	451.6	279.1	172.5	0.1000	0.0006
2067649	600	600.4	374.4	226	0.4000	0.0018
2067651	420.1	421.1	269.7	151.4	1.0000	0.0066
2067653	620.5	621	386.4	234.6	0.5000	0.0021
2067656	430.5	431.6	273.4	158.2	1.1000	0.0070
2067657	623.4	623.6	398.4	225.2	0.2000	0.0009
2067658	454.1	454.2	282.2	172	0.1000	0.0006
2067660	594.7	596	369	227	1.3000	0.0057
2067662	231.4	231.6	142.3	89.3	0.2000	0.0022
2067663	421	421.3	267.5	153.8	0.3000	0.0020
2067664	551	551.2	348.2	203	0.2000	0.0010
2067665	528.6	528.6	339.2	189.4	0.0000	0.0000
2067667	556.7	556.9	350.1	206.8	0.2000	0.0010
2067670	463.5	466.8	228.5	238.3	3.3000	0.0138
2067671	491.4	491.8	312.5	179.3	0.4000	0.0022
2067679	471.8	471.9	308.6	163.3	0.1000	0.0006
2067684	561.4	562.6	354.7	207.9	1.2000	0.0058
2067685	260.6	261.5	164.2	97.3	0.9000	0.0092

Continued on next page

Table 11 – *Continued from previous page*

Sample No.	$\mathbf{M}_{dry}$	$\mathbf{M}_{sat}$	$\mathbf{M}_{sub}$	$\mathbf{V}_b$	$\mathbf{V}_p$	ϕ
2067686	268.6	268.9	165.9	103	0.3000	0.0029
2067687	529.9	531.25	327.2	204.05	1.3500	0.0066
2067688	193.1	195.9	119.6	76.3	2.8000	0.0367
2067689	139.5	148	82	66	8.5000	0.1288
2067690	368.3	368.3	228.2	140.1	0.0000	0.0000

Table 12: Porosity of MMDD1

Sample No.	$\mathbf{M}_{dry}$ (g)	$\mathbf{M}_{sat}$ (g)	$\mathbf{M}_{sub}$ (g)	$\mathbf{V}_b$ (cm^3)	$\mathbf{V}_p$ (cm^3)	ϕ
2073745	2928.5	2941.4	1795.6	1145.80	12.90	0.0113
2073746	2332.8	2353.6	1420.2	933.40	20.80	0.0223
2073748	2274.4	2301.7	1375.7	926.00	27.30	0.0295
2073749	2729.8	2750.1	1645.5	1104.60	20.30	0.0184
2073750	2766.3	2793.4	1665.2	1128.20	27.10	0.0240
2073751	2001.5	2031.4	1196.1	835.30	29.90	0.0358
2073752	2201.4	2214.5	1387.4	827.10	13.10	0.0158
2073754a	1067.4	1070.9	681.3	389.60	3.50	0.0090
2073754b	1104.8	1113.2	699.4	413.80	8.40	0.0203
2073755	2116.5	2138.3	785.2	1353.10	21.80	0.0161
2073755a	625.8	639.1	389.8	249.30	13.30	0.0533
2073756	2236.4	2239.6	1416.9	822.70	3.20	0.0039
2073757	2036.6	2063.8	1265.9	797.90	27.20	0.0341
2073758	1815.9	1823.6	1143.3	680.30	7.70	0.0113
2073760	1174.5	1178.2	740.9	437.30	3.70	0.0085
2073761	1223.9	1226.1	785.2	440.90	2.20	0.0050
2073762	682.4	683.7	437.5	246.20	1.30	0.0053
2073763a	461.9	464	291.2	172.80	2.10	0.0122
2073763b	697.2	700.4	438.2	262.20	3.20	0.0122
2073764b	543.7	544.9	434.6	110.30	1.20	0.0109
2073765	692.2	697.9	440.1	257.80	5.70	0.0221
2073766	779	785.8	499.6	286.20	6.80	0.0238
2073767	910.7	918.9	585.1	333.80	8.20	0.0246

Continued on next page

Table 12 – *Continued from previous page*

Sample No.	M_{dry} (g)	M_{sat} (g)	M_{sub} (g)	V_b (cm^3)	V_p (cm^3)	ϕ
2073768	637.5	639.4	404.6	234.80	1.90	0.0081
2073769	592	593.1	378.2	214.90	1.10	0.0051
2073770a	642.9	645.3	406.6	238.70	2.40	0.0101
2073770b	478.3	480.3	302.7	177.60	2.00	0.0113
2073771	702	705	444.9	260.10	3.00	0.0115
2073772	1095.2	1098.5	699.5	399.00	3.30	0.0083
2073773	710.6	710.6	458.6	252.00	0.00	0.0000
2073774	1476.6	1478.7	930.6	548.10	2.10	0.0038
2073775	924.5	925.7	582.1	343.60	1.20	0.0035
2073776	1180.5	1181.1	741.5	439.60	0.60	0.0014
2073782	1485.9	1514.5	948.2	566.30	28.60	0.0505
2073783	1657.1	1683.2	1068.6	614.60	26.10	0.0425
2073784	1260.3	1280.6	804.1	476.50	20.30	0.0426